Atmospheric Research 231 (2020) 104652

Contents lists available at ScienceDirect

Atmospheric Research

journal homepage: www.elsevier.com/locate/atmosres

On the analysis of ground-based microwave radiometer data during fog conditions

Marouane Temimi[a,*], Ricardo Morais Fonseca[a], Narendra Reddy Nelli[a], Vineeth Krishnan Valappil[a], Michael John Weston[a], Mohana Satyanarayana Thota[a], Youssef Wehbe[a,b], Latifa Yousef[b]

[a] Khalifa University of Science and Technology, P.O. Box 54224, Abu Dhabi, United Arab Emirates
[b] National Center of Meteorology, Abu Dhabi, United Arab Emirates

ARTICLE INFO

Keywords:
Microwave radiometer
Radiation fog
Advection fog
Hyper-arid region
Planetary boundary layer

ABSTRACT

The goal of this study is twofold. First, we verify the retrievals of temperature and humidity profiles from a ground-based microwave radiometer (MWR) using radiosonde soundings. Second, we assess the potential of the MWR to nowcast fog formation and dissipation in a hyper-arid environment through the analysis of its profiles. The MWR is installed and operated at Masdar Institute in Abu Dhabi, United Arab Emirates (UAE), adjacent to Abu Dhabi's International Airport. MWR observations collected from 18 February 2017 to 31 March 2019.

A comparison with airport radiosonde data reveals a good agreement in particular for temperature, with the two measurements generally within 1 K from the surface to 10 km. For the specific humidity, the biases can reach 5 g kg^{-1} in the PBL. Biases can be attributed to errors in the radiosonde measurements and a non-optimized retrieval algorithm for the MWR.

A total of 14 fog events are identified during the study period. A strong near-surface inversion with lapse rates in the lowest 250 m of up to 30 K km^{-1} is needed for fog to form. Subsidence warming and drying associated with the subtropical anticyclone can descend down to 500 m, aiding the formation of fog at night. Cloud base height retrievals from the infrared (IR) camera capture fog onset and dissipation and complement the MWR observations. A synergy of different instruments could allow for more accurate fog detection.

1. Introduction

In the United Arab Emirates (UAE), fog is a major weather phenomenon that has the largest impact on the surface and air traffic. It occurs at a higher frequency than dust storms (e.g. Ali et al., 2013; Bartok et al., 2012), and the number of fog events in the UAE has increased in recent years as a result of changes in climate variability (Aldababseh and Temimi, 2017). This highlights the need to fully understand its mechanisms in order to improve the performance of operational forecasts and mitigate the associated negative impacts.

de Villiers and van Heerden (2007) and in Bartok et al. (2012) studied fog formation in the UAE and linked it to a combination of advective and radiative processes. During daytime the sea breeze brings in moist air from the Arabian Gulf that gets trapped at night within the stable boundary layer as a result of the land breeze and associated drop in wind speed (Al Azhar et al., 2016). Radiative cooling then leads to the formation of fog.

Given the different processes that are involved in the formation of fog, its prediction is rather challenging and numerical models often fail to simulate its occurrence, timing of onset and dissipation, and consequently its duration (e.g. Chaouch et al., 2017; Weston et al., 2018).

In general, short-term weather forecasting methods depend on the examination of stability/convective indices derived from upper air measurements to understand the evolution of thermodynamical parameters in the boundary layer (Feltz et al., 2003). However, the lack of continuous temperature and moisture profiles limits our understanding and operational forecasting techniques. In order to improve and properly evaluate operational fog forecasts, as well as enhance our current knowledge of the mechanisms behind its formation, high temporal and spatial resolution observational data is required. Unfortunately, such data is lacking over most of the UAE. The sources of observational data that are publicly available are the hourly Meteorological Aerodrome Reports (METARs) and the twice-a-day sounding data at the Abu Dhabi's airport. The radiosonde soundings provide snapshots of the

* Corresponding author.
E-mail address: marouane.temimi@ku.ac.ae (M. Temimi).

https://doi.org/10.1016/j.atmosres.2019.104652
Received 20 May 2019; Received in revised form 24 July 2019; Accepted 17 August 2019
Available online 19 August 2019
0169-8095/

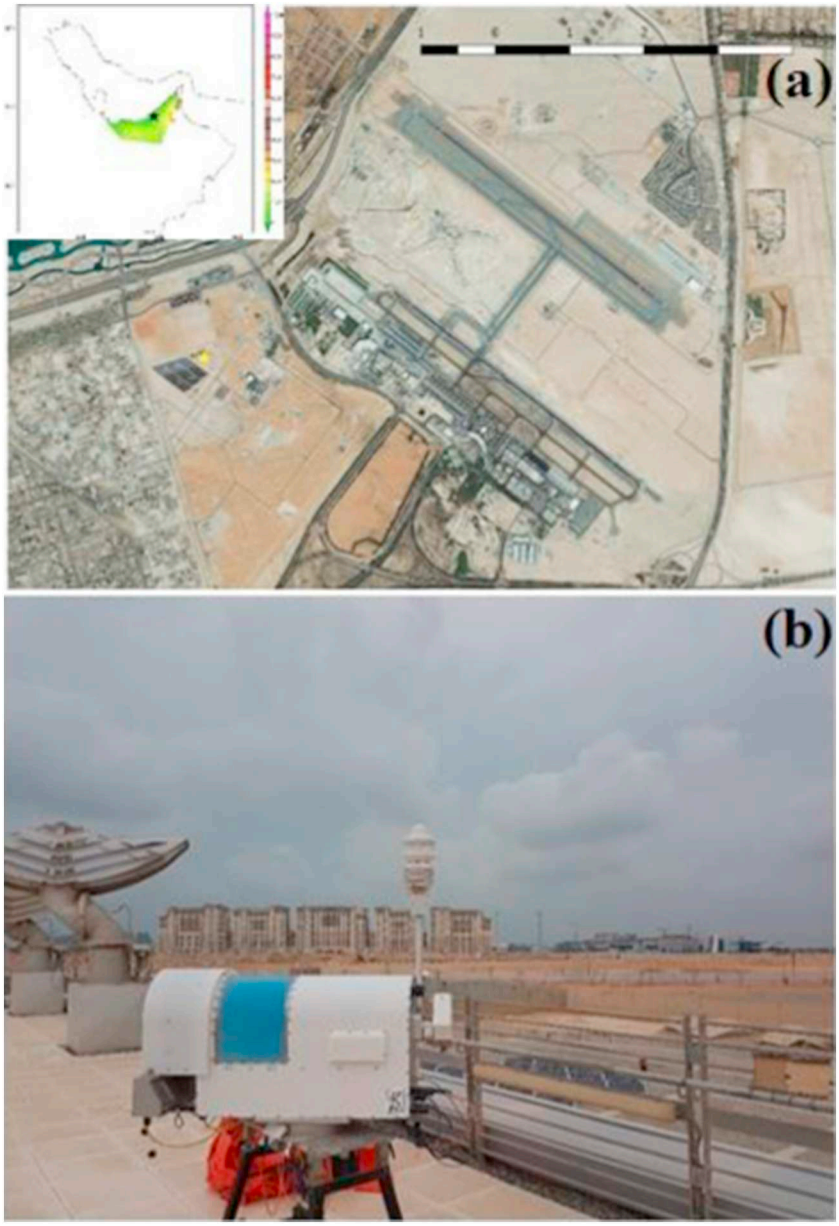

Fig. 1. (a) ArcGIS' aerial view with the airport located on the right and the MWR on the left (yellow star). The inset shows the 30-minute (spatial resolution of ~56 km) orography (m) of the UAE and the approximate location of the Abu Dhabi's International Airport (black star). (b) Photo of the MWR placed on the roof of a building within Masdar Institute. The integrated automatic weather station attached to the MWR is also seen. (For interpretation of the references to colour in this figure legend, the reader is referred to the web version of this article.)

state of the atmosphere twice a day which is informative, but clearly insufficient for continuous weather monitoring and nowcasting purposes. This is particularly critical for fog-related applications for which knowledge of the vertical profiles of temperature and moisture at a relatively high-temporal frequency is of paramount importance as conditions at the surface, and therefore, visibility can evolve rapidly (e.g. Chan and Li, 2018; Zhang et al., 2009). In addition, the available satellites with sounding sensors onboard, like AIRS and IASI for instance, have limited revisit time which does not allow for a continuous profiling of the atmosphere in near real time. Even though they are suitable to enhance the performance of numerical weather models through data assimilation, their coarse resolution and limited temporal coverage limit their use for the forecast and nowcast of local scale and surface level processes like fog formation and dissipation.

An alternative to space borne sounders is the ground-based microwave radiometer (MWR). It has the advantage of continuous monitoring of the atmosphere up to 10 km, filling the void created by conventional radiosonde measurements (Madhulatha et al., 2013). A MWR receives radiation emitted in the microwave band of the spectrum (K-band and V-band) from the atmosphere from which variables such as temperature, water vapour mixing ratio and relative humidity can be estimated (e.g. Bennartz and Bauer, 2003; Ming et al., 2019). This is normally achieved through linear/non-linear regression algorithms and artificial neural networks (e.g. Blackwell and Chen, 2009; Cadeddu et al., 2006). Provided that the measurements are calibrated, which is normally achieved by comparing the estimates with radiosonde data (e.g. John and Buehler, 2005; Zhang et al., 2018), the retrieved temperature and humidity profiles can help monitor the real-time development of fog events. It's worth noting that MWR supports different types of scans giving high vertical resolution temperature profiles for the Planetary Boundary Layer (PBL), which makes it useful for monitoring near surface changes in the atmospheric conditions including

fog-related applications (Knupp et al., 2009; Wærsted et al., 2017).

Several studies using MWR data have shown its potential to improve the nowcasting and forecasting of local weather processes. In a comprehensive field experiment, Chan (2009) demonstrated the importance of MWR profiles in nowcasting of convective weather. Later, Chan and Hon (2011) stressed the importance of MWR -derived stability indices in nowcasting intense convective weather over Hong kong. Madhulatha et al. (2013) examined the feasibility of using MWR data in nowcasting extreme weather events, such as thunderstorms, and concluded the need of a network of MWRs for operational forecasting. Nehrkorn and Grassotti (2003) have shown the improved fog onset prediction skill with the assimilation of raw radiometric brightness temperatures (rather than retrieved profiles). The MWR was used along with several other instruments in a thorough field campaign covering > 100 fog and near-fog events that took place in France in the winter of 2006–2007, ParisFOG (Haeffelin et al., 2010). The study revealed that turbulent coupling between the surface and the cloud base can explain the descending motion of the latter and subsequent formation of fog.

Despite the demonstrated potential of the instrument, the analysis of profiles obtained from MWRs showed in some cases noticeable discrepancies when compared to radiosonde profiles. For instance, a wet bias was reported by Cady-Pereira et al. (2008), Madhulatha et al. (2013), Westwater et al. (2003), when compared with radiosonde measurements. Also, Chan and Li (2010) noticed that the contamination of the background atmosphere causes the overestimation of cloud base height by the MWR. To our knowledge such assessment has never been done in a hyper-arid climate like the one in the UAE.

In this paper, measurements from a MWR installed in Abu Dhabi, a city located on the north-western coast of the UAE, are presented and evaluated against radiosonde soundings from the adjacent Abu Dhabi International Airport. A particular focus is placed on the analysis of the MWR data during fog events given their high frequency especially in the cold season. To the authors' knowledge, this is the first study that aims at evaluating retrievals from a MWR and investigating its potential in the prediction of the formation and dissipation of fog in a hyper-arid region. An understanding of the PBL environment prior, during, and after fog events is particularly important for the improvement of operational forecasts. This paper is structured as follows. In Section 2, the specifications of the MWR and that of the other instruments available at the field site, as well as the radiosonde data used to evaluate its performance, are presented. An evaluation of the MWR measurements is given in Section 3, while in Section 4 the focus is on the phenology of fog events. The main findings are summarized in Section 5.

2. Instruments and datasets

The MWR introduced in this paper is located at Masdar Institute, in the city of Abu Dhabi, UAE. Fig. 1(a) shows the location of the instrument (24° 26′ 11′ N, 54° 36′ 43″ E; approximately 27 m above mean sea level), roughly 4 km from Abu Dhabi's International Airport. At the airport, radiosonde ascents are taken twice daily at 00 and 12 UTC, the only location in the country where they are launched. Fig. 1(b) shows a photo of the radiometer that is placed on the roof of a building within Masdar Institute.

Observations were collected at least once every three minutes from 18 February 2017 to 31 March 2019. There are two gaps in the observation records, from 24 April to 1 November 2017, and 23 April 2018 to 5 February 2019. During these periods the instrument was not operational. Therefore, the available data records cover fully or partially three cold seasons in the UAE as follows: 18 February to 23 April 2017; 2 November 2017 to 24 April 2018; 6 February to 31 March 2019. Further details regarding the data availability are given in Fig. S1. The focus on fog events in this work is justified as the vast majority occur in the cold seasons, from November to February (Aldababseh and Temimi, 2017), when there is MWR data available for analysis.

A MWR, when compared to standard radiosondes, gives much higher vertical (and temporal) resolution profiles of temperature and water vapour mixing ratio, in particular at low levels just above the surface, where fog occurs. For example, and for the MWR used here, vertical profiles are generated at least every 5 min with roughly 31 levels in the lowest 1 km. This contrasts with the radiosonde measurements which are only available twice per day (at 00 and 12 UTC) and with up to 15 levels, but typically 5–10, in the bottom 1 km. Hence, the MWR measurements are crucial to better understand the mechanisms behind the formation and development of fog in this region. In addition to the MWR, a visibility sensor and an integrated automatic weather station are also available at the field site. In the next sub-sections, further details regarding all instruments are given.

2.1. Microwave radiometer: specifications

The RPG-HATPRO (G5 series) is a ground-based passive microwave radiometer, which operates in two frequency bands (Rose et al., 2005). It has seven channels in the K-band (22.24–31.40 GHz), for retrieving water vapour profiles, and seven channels in the V-band (51.26–58 GHz; oxygen band), for retrieving temperature profiles. RPG-HATPRO measures brightness temperatures at a temporal resolution of up to 1 s. It has two operation modes: zenith pointing (*Z*-mode) and elevation scanning mode (S-mode). In the Z-mode, the MWR points vertically, while in the S-mode it scans the atmosphere under elevation angles between about 4° and 90°. For the present study, temperature and humidity profiles from the Z-mode and S-mode are combined and used for analysis. They are available at least once every 5 min from the surface up to 10 km above ground level (AGL).

In order to obtain temperature and moisture profiles from the observed brightness temperatures, the radiative transfer equation has to be inverted which is normally achieved using statistical methods such as multiple regression, Bayesian estimation or neural networks (Chakraborty and Maitra, 2016; Panda et al., 2017). Here, the temperature and water vapour mixing ratio profiles are inferred from dual polarized observations at seven different frequencies using an artificial neural network (NN)-based approach (Jung et al., 1998; Crewell et al., 2001; Ying et al., 2011). The NN was trained prior to the deployment of the instrument using radiosonde profiles of temperature, pressure and humidity at Abu Dhabi, Muscat (Oman) and Dammam (Saudi Arabia) airport stations, as well European Centre for Medium Range Weather Forecasting Reanalysis (ERA-Interim) data (Dee et al., 2011). The cloud liquid water content from radiosonde profiles is estimated using a relative humidity threshold of 95% following Karstens et al. (1994). Once the profiles of temperature and moisture are obtained, related quantities such as the atmospheric stability and boundary layer height can be readily estimated.

The MWR is capable of measuring brightness temperatures in the range 0 to 800 K with a minimum accuracy of 0.5 K. The vertical resolution in the lowest 10 km of the atmosphere is always higher than 100 m, with vertical profiles of both temperature and humidity available on a second by second basis. This very high vertical and temporal resolution, combined with the blower system and heater module to prevent the formation of dew under fog conditions, make the instrument suitable for fog-related studies. Technical specifications of the MWR are given on the manufacturer's website (HATPRO, 2019).

In boundary layer mode, the radiometer scans the atmosphere 0° Azimuth angle for different elevations (0°, 4.2°, 4.8°, 5.4°, 6.6°, 8.4°, 11.4°, 14.4°, 19.2°, 30.0°) to get the accurate and high resolution temperature profiles in the PBL. The RPG-HATPRO uses integration times of 20–60 s per angle (user selectable) with a total scan time of 2–6 min. During the BL scan (S mode), the zenith scan (Z mode) observation is disabled. In the present study, BL scan time of 2 min with a repetition period of nearly 15 min is adopted. Four channels, 51.26, 52.28, 53.86, 54.94 GHz, are used to retrieve the boundary layer temperature profiles during boundary layer scan.

The MWR is also equipped with an infrared temperature sensor

(IRTS) that gives an estimate of the cloud base height (CBH) and cloud liquid water. The IRTS sensor is sensitive to radiation in the 8 to 14 μm band, where the absorption of water vapour and carbon dioxide is weak. It is installed along with the MWR in order to improve the atmospheric transmittance and hence the accuracy of the cloud radiation measurements (Wang et al., 2018). The IRTS measurements are combined with the MWR observations to improve the estimated humidity vertical profiles (RPG, 2019).

Retrievals from the MWR are compared to radiosonde profiles obtained from Abu Dhabi's International Airport, Fig. 1(a), that is adjacent to Masdar Institute site where the MWR is deployed. Radiosondes are launched twice daily at 00 and 12 UTC. This is the only location in the UAE where radiosondes are launched. The radiosonde profiles used here were downloaded from the University of Wyoming's website (University of Wyoming, 2019).

2.2. Surface observations

The visibility sensor, Sentry™ SVS1, estimates the scattering of visible light by the atmosphere from which the extinction coefficient μ (amount of attenuation of a beam due to scattering and absorption by aerosols) is calculated. From this measurement, the visibility (v), a particularly useful quantity for fog-related applications, can be readily estimated. This is done separately for daytime and nighttime conditions through the equations below. Technical specifications of the visibility sensor are provided on the manufacturer's website (SENTRY™, 2019).

$$v = \frac{3}{\mu} \text{ (day time)}$$

$$v = e^{-\frac{\mu v}{0.00336}} \text{ (nighttime)}$$

An integrated automatic weather station, Lufft® WS600-UMB, which comprises a wind, precipitation, pressure, temperature and relative humidity sensor, is available with the MWR and can be seen in Fig. 1(b). Technical specifications of the different weather sensors are available on the manufacturer's website (WS600-UMB, 2019).

3. Evaluation of the MWR vertical profiles

In this section, the temperature (T) and specific humidity (q) profiles given by the MWR are evaluated against the vertical profiles from radiosondes launched at Abu Dhabi's International airport. The close proximity of the MWR to the radiosonde launch site, roughly 4 km as evidenced in Fig. 1(a), makes it justifiable to directly compare the two sets of observations.

Fig. 2 shows the average temperature and specific humidity vertical profiles at 00 and 12 UTC from radiosonde and MWR. The individual MWR and radiosonde profiles used to construct Fig. 2 were first visually checked with the outlier (physically not meaningful) profiles are discarded. The procedure, yielded, a total of 243 profiles for 00 UTC and 246 profiles for 12 UTC, which were used for further analysis. The two temperature profiles are in close agreement in particular at 00 UTC (4 a.m. local time), when an inversion is seen at roughly 500 m. Nighttime near-surface inversions are a common occurrence in arid regions like the UAE (Lazzarini et al., 2014). Above the inversion, the temperature drops at an average rate of 6.7 K km^{-1}, which is close to the typical environmental lapse rate of 6.5 K km^{-1}. At 12 UTC (4 p.m. local time), both the radiosonde and MWR profiles show a decrease in temperature in the bottom 10 km of the atmosphere, at an average rate of 6.7 K km^{-1}. The main difference between the two is at very low heights just above the surface, where the radiosonde profile shows a super-adiabatic lapse rate (> 10 K km^{-1}) and a surface temperature of about 302.5 K, while the MWR profile gives a surface temperature of about 299.5 K and a lapse rate close to 7 K km^{-1}.

Overall, the temperature differences are small, generally within 1 K, indicating that the measurements by the two instruments are very similar up to 10 km. The exception is at 12 UTC and at very low levels just above the surface. A possible explanation is that the black asphalt pavement at the airport leads to higher surface temperatures and a steeper near-surface lapse rate when compared to the reflective white stone surface where the MWR is placed (Picón-Feliciano et al., 2009).

In contrast to the temperature, specific humidity profiles from the two measurements are different. In the radiosonde profiles at 00 UTC and 12 UTC there is a steady decrease of moisture with height up to 2 km, at steeper rate at lower elevations. The MWR profile, on the other hand, shows a sharp decrease in moisture below 500 m, followed by nearly constant values at up to 1–1.5 km. These tendencies are more significant at 12 UTC. Above 500 m, the specific humidity increases up to 3 km and decreases again for higher heights. In other words, in the MWR profile, when compared to the radiosonde profile, there is a drier layer in the lowest 1.5–2 km, and a more moist layer between 2 km and 6 km. A similar pattern of errors has been reported by other authors such as Chan (2009), Xue and Eltahir (2015), Zhang et al. (2018) for measurements taken in Hong-Kong, Wuhan (China) and equatorial Indian Ocean, respectively. Over India, while Balaji et al. (2017) reported a similar pattern. Madhulatha et al. (2013) and Ratnam et al. (2013) found tendencies of the opposite sign: a wet MWR bias at low-levels, and a dry MWR bias in the mid- and upper-troposphere.

The drier and slightly warmer radiosonde profiles in the mid-troposphere can be explained by the solar heating of the humidity sensor used in the Väisälä radiosondes (Turner et al., 2003; Vömel et al., 2007). This is consistent with the fact that the referred biases are more reduced at night. At very low levels, the radiosonde measurements are of higher quality.

As the averaging is done over daytime and nighttime, the humidity biases in the bottom 2 km suggest that the radiative transfer model employed by the MWR probably has to be further refined for this region. The need to optimize the retrieval algorithm accounting for the peculiarities of the specific instrument and atmospheric conditions has been stressed by several authors such as Zaitsev et al. (2014). Such an improvement of the retrieval algorithm is outside the scope of this study. It is also important to note that while the MWR is fixed in space, a radiosonde should drift along with the wind, and hence a perfect agreement between the two sets of measurements is not expected in particular for the humidity fields that exhibits a larger variability than the temperature.

In Fig. 3, the bias profiles of T and q for individual months are plotted separately. The Root-Mean-Square-Error (RMSE) for the lowest 2 km, representative of the PBL conditions, and between 2 and 10 km, representative of the free atmosphere, is given in Table 1. The mean bias and RMSE in T and q are comparable between the months, within the PBL for T and throughout the troposphere for q. In the lower atmosphere, the temperature biases (and the RMSE values) are rather small, generally within 2 K. However, in the free troposphere, they are larger, exceeding 4 K for some of the months for heights above 6 km. This discrepancy is likely related to deficiencies in the retrieval algorithm, as the brightness temperatures for the months of December and February are comparable to those for January (not shown). A non-optimized retrieval algorithm can also explain the general increase in the temperature biases from November to April, with the MWR-estimated temperature being mostly lower than that obtained from radiosondes from November to January, and mostly higher in March and April. It is important to stress that the larger magnitude biases at higher elevations may also arise from the fact that at lower heights measurements from both the zenith pointing (Z-mode) and elevation scanning (S-mode) modes are used, whereas for higher heights, only data from Z-mode scans are available, which may result in less accurate retrievals. Despite the larger magnitude of the temperature biases for the individual months, however, the fact that they have opposite signs means that the overall averaged temperature bias will be small. The specific humidity biases and RMSEs can be as large as 6 g kg^{-1} and 5 g kg^{-1} in the lower atmosphere, respectively, with the magnitudes reduced generally by

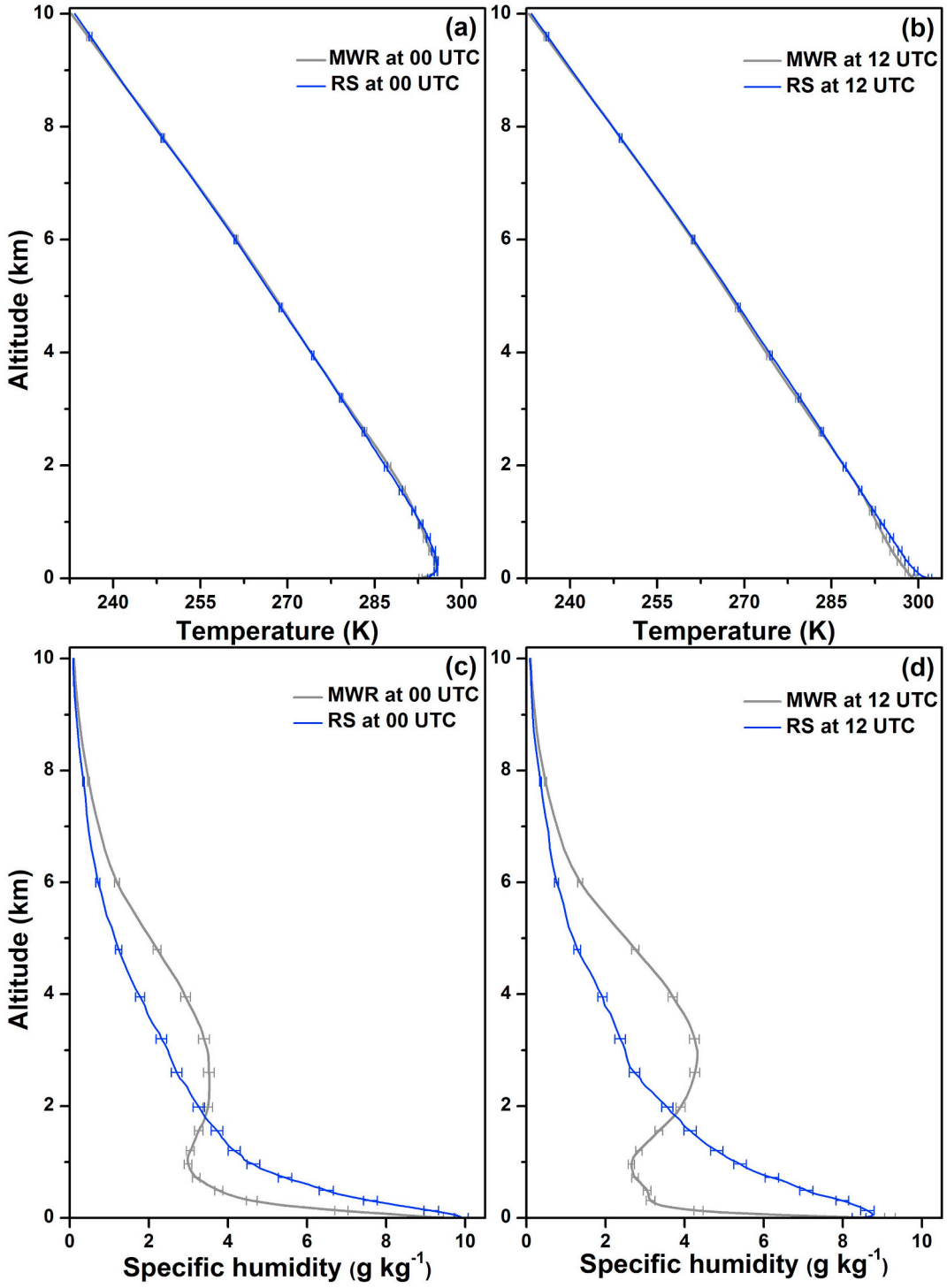

Fig. 2. Vertical profiles of air temperature (K) at (a) 00 UTC and (b) 12 UTC for the MWR and radiosonde averaged over the full study period. (c) and (d) are as (a) and (b) but for specific humidity (g kg^{-1}). The error bars indicate the standard deviation of the mean.

more than a factor of two in the free atmosphere. Table 1 also shows the scores for the relative humidity. By and large the tendencies are the same as for T and *q*, with the larger magnitudes probably arising from the uncertainties in the radiosonde relative humidity measurements (e.g. Turner et al., 2003; Vömel et al., 2007).

It is important to note that, as stated in Section 2.1, radiosonde data from Abu Dhabi's International Airport was used by the manufacturer to calibrate the MWR. To estimate the temperature and humidity profiles, a relationship was developed using radiosonde observations and simulated brightness temperatures from ERA-Interim atmospheric profiles. One should assume that the deployment of the MWR at a site adjacent to where the radiosonde data used for the calibration were obtained should lead to accurate retrievals. However, the bias in the ERA-Interim atmospheric profiles and the errors introduced by the forward radiative modeling to simulate the instrument's brightness temperatures contribute to the biases in the MWR profiles.

Figs. 3(c)–(d) that show the specific humidity bias indicate that the bias is consistent and does not show a significant monthly variability in both phase (i.e. shape of vertical profile) and magnitude. Hence, the mean profiles for each month are used to bias correct the MWR specific

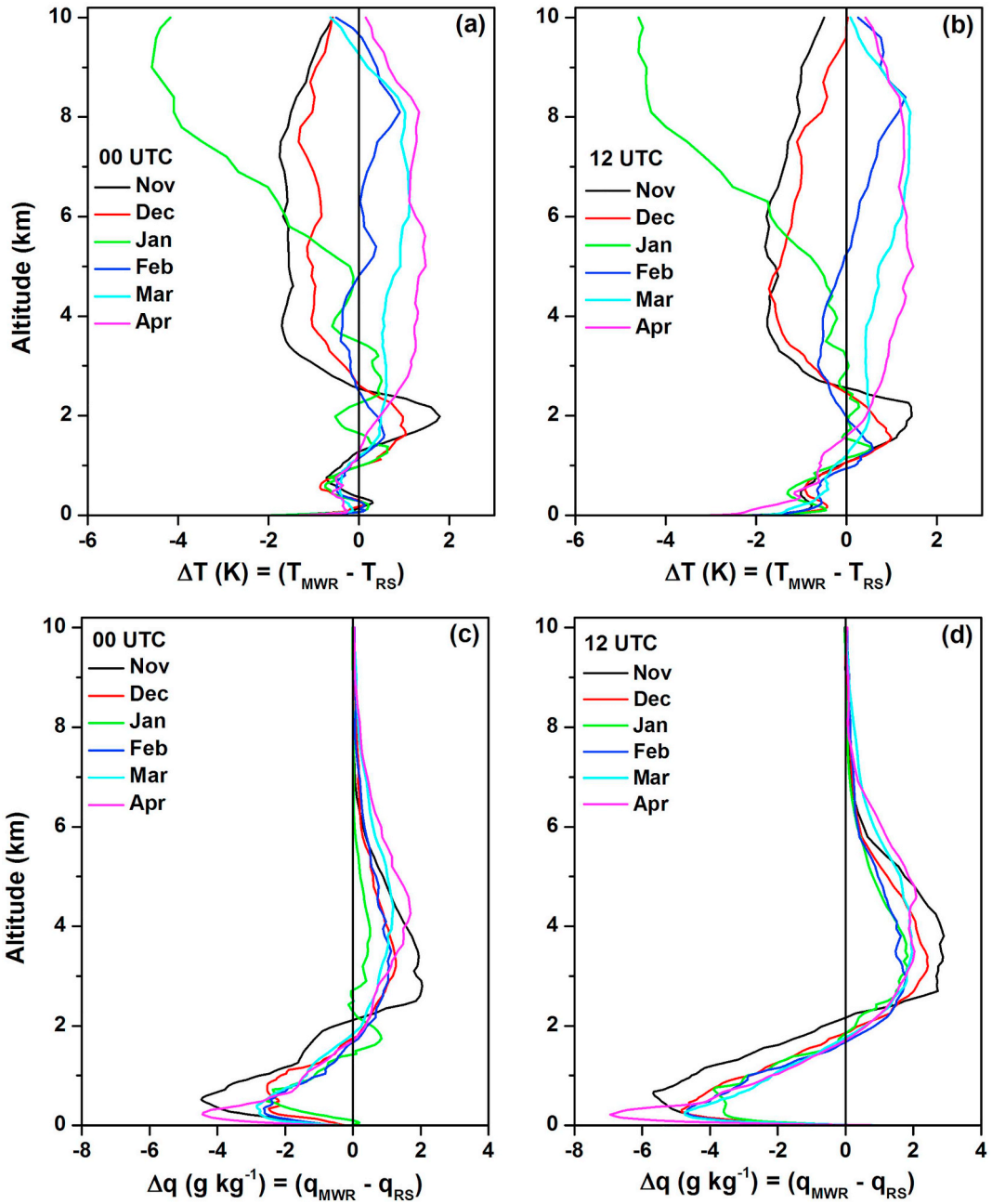

Fig. 3. Bias between the MWR and radiosonde (a) temperature (K) and (b) specific humidity (g kg^{-1}) vertical profiles at 00 and 12 UTC for each of the months considered in this study. The conventions are as in Fig. 2.

Table 1
Mean RMSE between the MWR and radiosonde air temperature (K), specific humidity (g kg^{-1}), and RH (%) profiles for the boundary layer (altitudes < 2 km) and free atmosphere (altitudes between 2 and 10 km) at 00 UTC and 12 UTC.

Month	RMSE in air temperature (K)		RMSE in specific humidity (g kg^{-1})		RMSE in RH (%)	
	< 2 km	2–10 km	< 2 km	2–10 km	< 2 km	2–10 km
	00/12 UTC	00/12 UTC	00/12 UTC	00/12 UTC	00/12 UTC	00/12 UTC
November	0.9/1.1	1.9/1.9	3.3/4.5	1.2/1.7	19.5/25.4	19.1/26.8
December	1.0/1.0	1.6/1.6	2.3/3.6	0.9/1.4	19.0/26.1	19.4/26.1
January	1.1/1.2	2.5/2.7	1.9/2.9	0.4/1.0	18.8/24.2	10.2/18.8
February	1.0/1.2	2.4/2.4	2.3/3.4	1.0/1.3	18.6/23.5	21.8/25.9
March	1.0/1.3	2.8/2.8	2.6/3.1	1.1/1.5	17.5/17.5	18.8/24.2
April	1.3/1.4	2.9/2.7	3.2/3.7	1.2/1.6	15.0/16.0	19.6/24.8

humidity observations used in the subsequent analysis. A more sophisticated bias correction approach could be applied to alter the MWR profiles in real time. This is beyond the scope of this study.

The MWR temperature and humidity vertical profiles are analysed to gain further insight into the capability of the instrument in sensing the local atmospheric conditions at the site, with a focus on the Planetary Boundary Layer (PBL). The focus will be on the bottom 2.5 km of the atmosphere, where fog-related processes take place and the MWR provides much increased vertical resolution compared to the radiosonde profiles. The MWR is a potential tool for monitoring the PBL structure including its depth (Cimini et al., 2013). The analysis accounts for the characterized biases in the previous section.

There are various ways to estimate the PBL height that make use of vertical profiles of air temperature, potential temperature, virtual potential temperature v, and/or specific humidity q (e.g. Basha and Ratnam, 2009). In the present study, a simple gradient method applied to the vertical profile is used to estimate the PBL depth (Garratt, 1992). The PBL depth is defined as the height z in the bottom 5 km at which dθ/dz. is maximized. As discussed in Seidel et al. (2010), the choice of the method used to estimate the PBL depth may yield differences of up to a few hundred meters and will not change qualitatively the findings reached in the analysis.

Typical profiles of dθ/dz during daytime (1130 Local Time (LT)) and nighttime (2230 LT) taken on 29 March 2019 are shown in Fig. 4(a) and (b), respectively. In order to smooth the potential temperature gradient profile, a nine-point moving average is applied. The diurnal cycle of the PBL depth averaged over all the study period is given in Fig. S2.

At night, a strong temperature inversion is present with a rather shallow PBL which has a depth of about 160 m. Such thermal inversions are a regular occurrence in the region (Lazzarini et al., 2014). In contrast, at 11:30 LT, there is a close to well-mixed layer just above the surface in the bottom 200 m (i.e. is roughly constant with height), and a stable layer above. At this time of the day the PBL top is at roughly 1.12 km. For both daytime and nighttime profiles, and for heights above about 1.5 km, dθ/dz. is very small, close to zero. This indicates that the temperature lapse rate is close to the dry adiabatic value of $\sim 9.8\ \mathrm{K\,km^{-1}}$, with slightly warmer potential temperatures during the day.

Fig. 5 shows the evolution of the temperature and humidity fields for the same day. For this particular day, the sunrise was at 0616 LT and the sunset at 1837 LT. As noted in Fig. 4, a temperature inversion develops after sunset around 21 LT, and is present throughout the night. The resulting shallow boundary layer traps moisture underneath, with the water vapour mixing ratio in the late evening and early hours exceeding $13\ \mathrm{g\,kg^{-1}}$. The cooler and more moist nighttime environment, in particular in the cold season, favors the formation of fog (Aldababseh and Temimi, 2017). Roughly 2–3 h after sunrise, around 8–9 LT, the nighttime inversion is fully eroded, with the merging between the mixed layer and the residual layer from the previous night producing a sudden increase in the PBL depth after 10 LT, in line with that reported by other authors (e.g. Blay-Carreras et al., 2014). The deeper PBL and resulting enhanced vertical mixing lead to drier conditions near the surface and moister conditions aloft at roughly 500–1000 m, just below the boundary layer top. An inspection of Fig. 5(b) reveals that, at night, the atmosphere is statically stable, as the potential temperature θ increases rapidly with height. Conversely, around 12–14 LT, θ is nearly constant in the bottom 750 m indicating a well-mixed environment. In the transition between the two regimes in the morning, mostly around 10–12 LT, the near-surface profile is unstable, with a super adiabatic temperature lapse rate. Around 22–24 LT and 4–6 LT, and mostly in the layer 300–600 m, there is a warming and drying of the atmosphere, possibly arising from subsidence associated with the subtropical anticyclone (e.g. Seager et al., 2003), as evidenced by the vertical (downward) advection of higher values of θ.

Regarding the evolution of the PBL, it is deeper during daytime, as a result of the strong heating of the surface by the Sun, with a maximum depth of about 1–1.2 km from about 11–17 LT. In the evening and nighttime hours, it is rather shallow, with depths below 0.3 km. This diurnal variability is representative of that seen at other times of the year, and is also in line with that reported by other studies (e.g. Eager et al., 2008). While the evolution of the low-level atmosphere and the stable boundary layer depth for this site is similar to that observed at other arid and semi-arid sites, the daytime boundary layer depth is noticeably reduced. For example, Qiang et al. (2006), Qiang and Sheng (2009), Zhang et al. (2011) and Wang et al. (2016) for a desert in northwestern China, Kumar et al. (2010) for a semi-arid region in India, and Garcia-Carreras et al. (2015) for the Saharan Desert, estimated maximum depths that can exceed 4 km. A possible explanation is the more moist atmosphere at Abu Dhabi, a result of the advection of moist air from the neighbouring Arabian Gulf which, in the summer, has one of the highest sea surface temperatures of any water body in the world (e.g. Eager et al., 2008; Xue and Eltahir, 2015).

The occurrence of condensation near the soil surface level right before fog formation leads to an increase of soil moisture in the top layer of the soil (few millimeters to centimeters; Fares et al., 2013; Temimi et al., 2014; Al Jassar et al., 2019). This should affect the heat fluxes, turbulences, and PBL height (Fig. 5). In a recent study, Wehbe et al. (2018) simulated the impact of accounting for land-atmospheric feedbacks in the surface energy balance over the hyper-arid

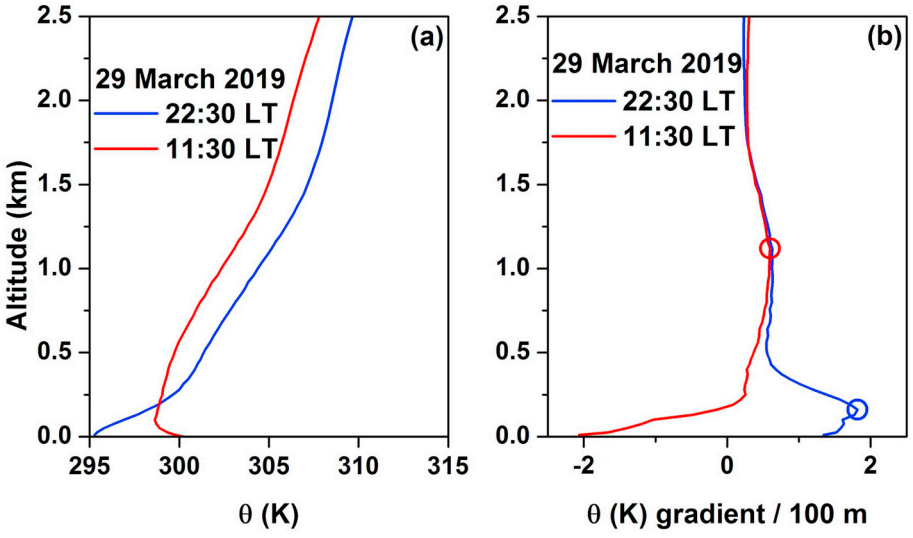

Fig. 4. Typical profiles of (a) potential temperature (K) and (b) potential temperature gradient (K/100 m) during daytime (red) and nighttime (blue) hours on 29 March 2019. The PBL height is marked by an open circle in (b), and is roughly 0.16 km at 2230 LT and 1.12 km at 1130 LT. (For interpretation of the references to colour in this figure legend, the reader is referred to the web version of this article.)

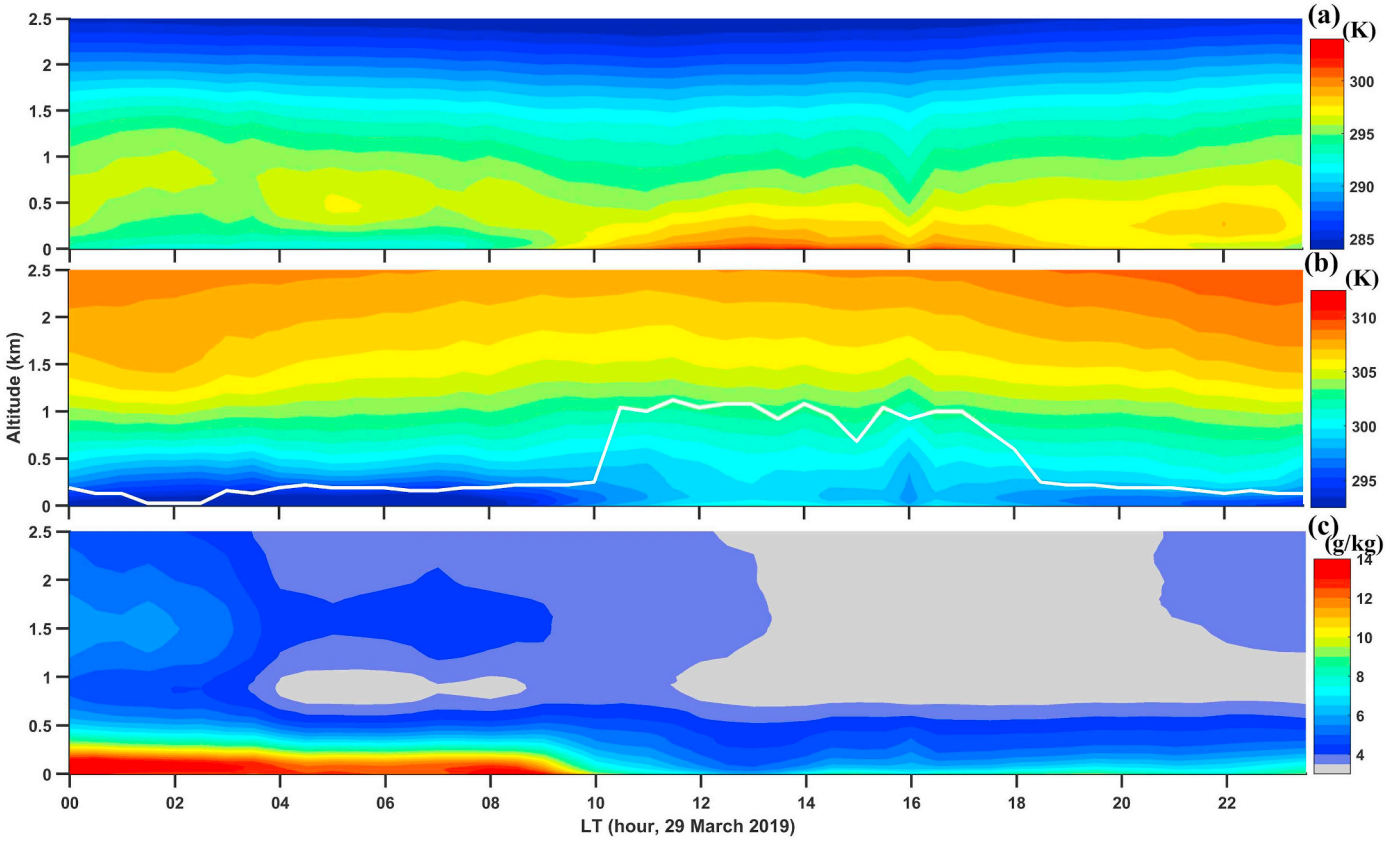

Fig. 5. Diurnal variability of the (a) temperature (K), (b) potential temperature θ (K), and (c) bias-corrected (see text for more details) specific humidity (g kg^{-1}) from surface to 2.5 km altitude on 29 March 2019. The thick white line in (b) highlights the boundary layer depth, defined as the height in the bottom 5 km at which the potential temperature vertical gradient is maximized. The potential temperature profiles at 11:30 LT and 22:30 LT are given in Fig. 4.

environment of the UAE. Standalone (atmospheric) model runs were compared to fully-coupled (land-atmospheric) runs to isolate and diagnose the soil moisture-precipitation feedback mechanisms proposed by Eltahir (1998), Wehbe et al. (2017, 2019). The soil moisture in the top layer was found to decrease both the surface albedo and the Bowen ratio. The reduced surface albedo caused more absorbance of net radiation, while the reduced Bowen ratio was attributed to higher water vapour content in the boundary layer and more downwards flux of terrestrial radiation at the surface from the water vapour greenhouse effect. The combined effect amounted to the release of a larger total heat flux from the surface into the boundary layer. In line with the present study, the cooling of the surface temperature accompanied by the increase in near surface condensation, and consequently, soil moisture prior to fog, was associated with a collapse of the PBL.

4. Analysis of fog conditions

Fog in the UAE forms through a combination of advective and radiative processes. The sea breeze brings in moist air from the Arabian Gulf that is then trapped at night when the land breeze kicks in and the wind speed drops. Radiative cooling, in particular in the winter season when it is more pronounced, is the final ingredient needed for the formation of fog. Among the various types of fog, the radiation type is predominantly seen in the winter months from November to February (e.g. de Villiers and van Heerden, 2007). It is worth noting that the thinning or absence of clouds during nighttime increases the likelihood of radiation fog formation (Meyer and Lala, 1990). Yousef et al. (2019) conducted a study on cloud cover over the UAE, using ground observations taken at the major international airports. Frequency analysis on the amounts of cloud cover reported showed that during nighttime, lower amounts are reported more frequently. Further studies on diurnal cloudiness have indicated higher cloudiness occurring in the morning period for the Arabian Peninsula, with lower amounts occurring at night (Foster and Heidinger, 2012; Uwe et al., 2012).

Fig. 6 shows the temperature and humidity profiles for the period 12 LT 21 December to 12 LT on 24 December 2017, when two fog events occurred: a short one from 0222 to 0928 LT on 22 December, and a longer one from 2004 LT on 22 December to 1025 LT on 23 December. These onset and dissipation times, which are highlighted in Fig. 6 with white dashed -dotted and dashed vertical lines, correspond to the times when the visibility sensor readings dropped below 1000 m (Fig. S3), and roughly match the onset and dissipation fog times according to the METAR data from the nearby airport (Table 2). The measurements taken by the sensors in the integrated weather station are given in Fig. 7.

An analysis of Fig. 6 reveals that, during the fog events, the nighttime near-surface temperature inversion is stronger and longer lasting compared to non-foggy conditions on 24 December. For example, the lapse rate in the lowest 250 m can be as high as 30 K km^{-1} and exceeds 9.8 K km^{-1} for at least 8 h in the first two nights when fog formed. Conversely, on the night of the 24 December when fog does not occur, this lapse rate does not exceed 17 K km^{-1}, and is only higher than 9.8 K km^{-1} for about 2 h. In other words, the strength and the persistence of the near-surface temperature inversion seems to be a factor that controls fog development. This is consistent with observations made at other sites (RenHe et al., 2014). For the two fog events considered here, the inversion forms about 3–5 h before the onset of fog and can be as deep as 800 m.

Fig. 6 shows that the warmer (and drier) daytime air is lifted upwards during late afternoon and evening hours, and remains above the nighttime stable layer overnight, with radiative cooling reducing the temperature by a couple of degrees. This residual layer is characterized

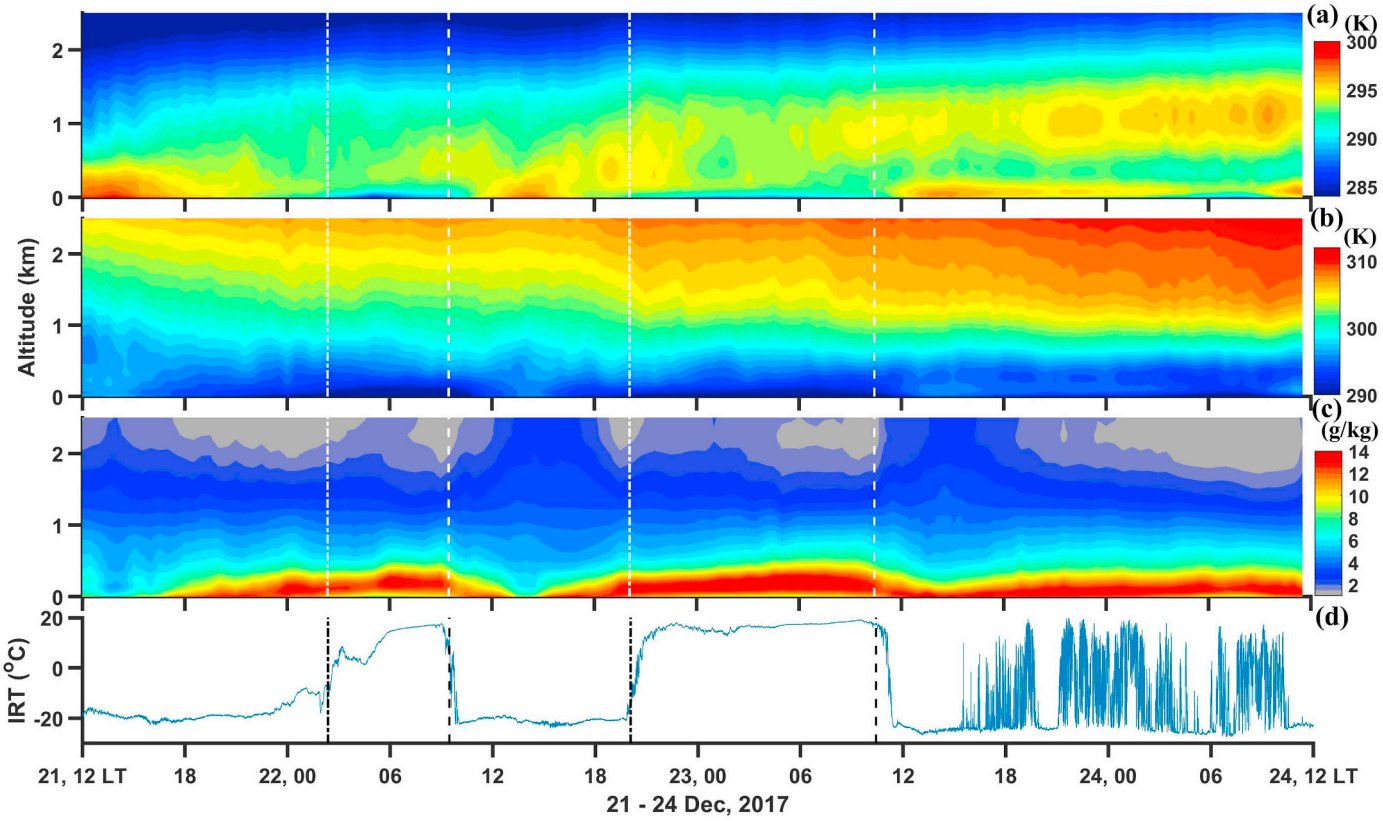

Fig. 6. Phenology of two fog events on 22 and 23 December 2017 as observed by the MWR. Shown are the (a) temperature (K), (b) potential temperature (K), (c) bias-corrected specific humidity (g kg^{-1}) vertical profiles from surface to 2.5 km altitude, and (d) brightness temperature (K) from the IRTS for the period 12 LT on 21 to 12 LT on 24 December 2017. The vertical dot-dashed and dashed lines denote the periods when fog occurred at the site: i.e., when the visibility, as given by the visibility sensor, dropped below 1000 m (see Fig. S3 for more details).

Table 2
Onset and dissipation times and duration of fog events which occurred during the period for which MWR data is available and lasted > 1 h. The last two columns show the averaged visibility (km) and PBL depth (km) over the entire fog event. For each event, two sets of values are given: the top value is taken from METAR data, and the bottom from the visibility sensor in the field site. Measurements from the visibility sensor are not available on 2 March and 23 April 2017.

S. No.	Onset time (LT)	Dissipation time (LT)	Duration (h)	Visibility (km)	PBL depth (km)
1	02/03/17 at 03:01 LT	02/03/17 at 08:06 LT	5 h 5 min	0.508	0.025
	—	—	—	—	
2	23/04/17 at 06:05 LT	23/04/17 at 07:11 LT	1 h 6 min	0.533	0.220
	—	—	—	—	
3	22/12/17 at 03:00 LT	22/12/17 at 09:00 LT	6 h	0.189	0.025
	22/12/17 at 02:22 LT	22/12/17 at 09:29 LT	7 h 7 min	0.217	
4	22/12/17 at 20:34 LT	23/12/17 at 10:37 LT	14 h 3 min	0.227	0.025
	22/12/17 at 20:04 LT	23/12/17 at 10:34 LT	14 h 30 min	0.188	
5	25/12/17 at 03:07 LT	25/12/17 at 09:42 LT	6 h 35 min	0.259	0.025
	25/12/17 at 02:59 LT	25/12/17 at 09:25 LT	6 h 26 min	0.193	
6	26/12/17 at 01:25 LT	26/12/17 at 07:12 LT	5 h 47 min	0.319	0.025
	26/12/17 at 01:36 LT	26/12/17 at 08:18 LT	6 h 42 min	0.191	
7	06/02/18 at 07:43 LT	06/02/18 at 09:00 LT	1 h 17 min	0.525	0.025
	06/02/18 at 06:16 LT	06/02/18 at 08:52 LT	2 h 36 min	0.398	
8	07/02/18 at 05:32 LT	07/02/18 at 09:24 LT	3 h 52 min	0.371	0.025
	07/02/18 at 06:28 LT	07/02/18 at 09:42 LT	3 h 14 min	0.234	
9	08/02/18 at 04:11 LT	08/02/18 at 10:40 LT	6 h 29 min	0.254	0.025
	08/02/18 at 04:15 LT	08/02/18 at 10:11 LT	5 h 56 min	0.196	
10	10/02/18 at 02:11 LT	10/02/18 at 09:30 LT	7 h 19 min	0.236	0.025
	10/02/18 at 00:18 LT	10/02/18 at 09:46 LT	9 h 28 min	0.236	
11	16/03/18 at 04:00 LT	16/03/18 at 08:00 LT	4 h	0.233	0.025
	16/03/18 at 03:47 LT	16/03/18 at 09:07 LT	5 h 40 min	0.275	
12	07/03/19 at 05:44 LT	07/03/19 at 09:00 LT	3 h 16 min	0.538	0.025
	07/03/19 at 06:36 LT	07/03/19 at 08:32 LT	1 h 56 min	0.349	
13	14/03/19 at 06:00 LT	14/03/19 at 08:00 LT	2 h	0.400	0.160
	14/03/19 at 06:22 LT	14/03/19 at 07:53 LT	1 h 31 min	0.342	
14	29/03/19 at 03:37 LT	29/03/19 at 07:42 LT	4 h 5 min	0.590	0.190
	29/03/19 at 05:42 LT	29/03/19 at 07:19 LT	1 h 37 min	0.536	

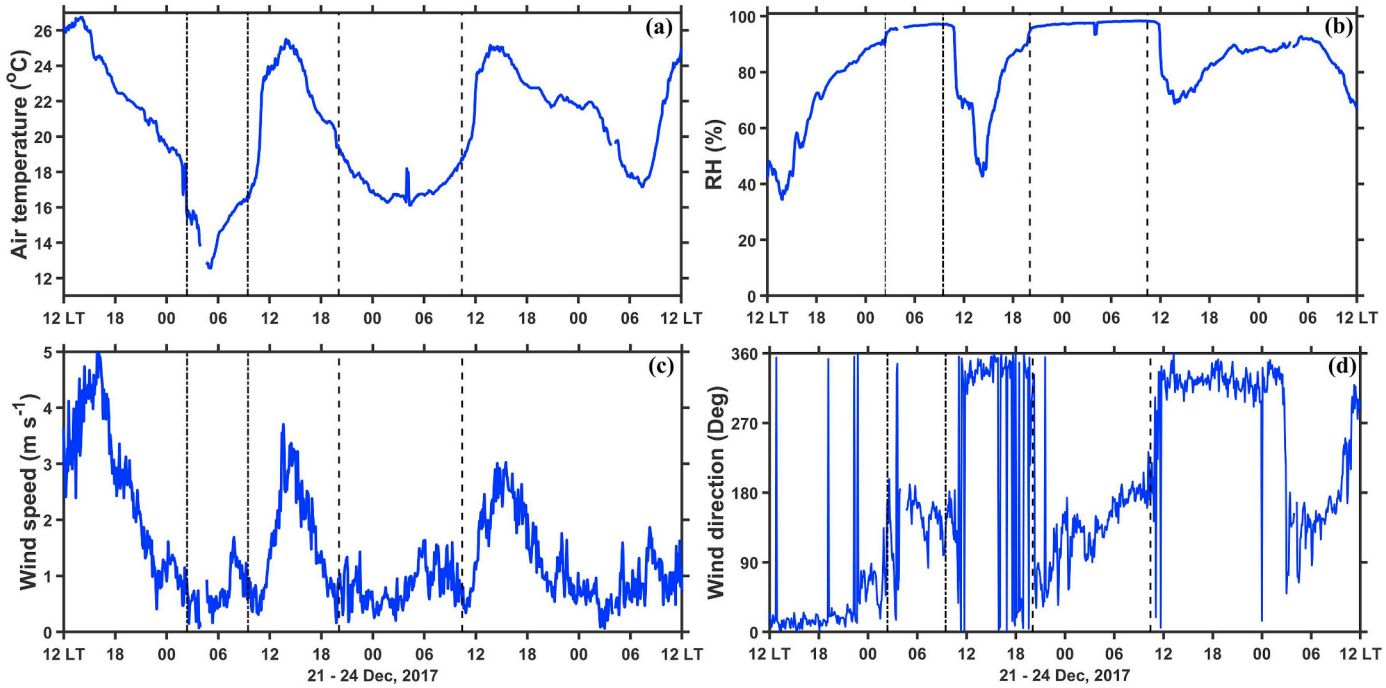

Fig. 7. Surface meteorological parameters from the integrated weather station for the period 12 LT on 21 to 12 LT on 24 December 2017. Shown are the (a) air temperature (°C), (b) Relative humidity (%), and horizontal wind (c) speed ($m\,s^{-1}$), and (d) direction (°). The dot-dashed and dashed lines denote the periods when fog occurred: i.e., when the visibility, as given by the visibility sensor, dropped below 1000 m.

by a weak vertical potential temperature gradient (i.e. low $d\theta/dz$) as seen in Fig. 6(b). On 23 and in particular on 24 December, a layer of strong subsidence descends from 2.5 km to roughly 1 km, as seen by the downward advection of higher θ values, with the associated adiabatic warming leading to warmer and drier conditions. As a result, the depth of the residual layer is reduced to < 500 m at the end of the 3 -day period. Large-scale subsidence is a common occurrence in this region, where the subtropical anticyclones play a dominant role in the weather conditions throughout the year (Seager et al., 2003).

An inspection of the specific humidity profile shows a gradual increase in the near-surface water vapour mixing ratio in the afternoon and evening hours. This results from the advection of night moisture from the Arabian Gulf by the sea-breeze circulation (Chaouch et al., 2017; Weston et al., 2018), shown in Fig. 7(c) and (d) by the predominantly northerly to north-westerly winds and increased wind speeds. The amount of water vapour in the bottom 250 m does not seem to be correlated with the occurrence of fog: the highest specific humidity values at the surface are measured at 1330 LT on 23 December, ~14 $g\,kg^{-1}$, but no fog formed overnight on 24 December. The very moist near-surface air with a specific humidity in excess of 10 $g\,kg^{-1}$ is lifted above the nighttime stable layer, and mixes downwards to the surface during the morning (roughly between 6 LT and 12 LT) when the inversion is destroyed. The lowering of the nocturnal residual layer has been reported by other authors (e.g. Fochesatto et al., 2001; Muñoz and Undurraga, 2010). Overnight a shallow drier layer develops just above the surface, with a relative reduction in the water vapour mixing ratio with respect to the maximum evening value of roughly 40%, 33% and 36% for the three days. A possible explanation is condensation and formation of dew (or fog) that acts to reduce the amount of available water vapour in the atmosphere. This is a common occurrence in arid regions in particular in the cold season as a result of the strong radiative cooling during nighttime hours (e.g. Jacobs et al., 2000). As seen in Fig. 7(c), during the fog events the wind speed is very low but not zero, around 0.5–1.5 $m\,s^{-1}$. This is consistent with Payra and Mohan (2014) who stressed that a slight amount of turbulent mixing aids the formation of fog. The sudden and short-lived increase in air temperature during the second fog event, around 04 LT on 23 December, may result from condensation (and subsequent latent heat release) on the surface of the sensor with the water quickly evaporating into the air.

The fog period on 23 December was roughly twice as long as that on 22 December. From the evolution of the humidity profiles shown in Fig. 6(c), on 22 December near the fog top there appears to be enhanced vertical mixing with the drier adjacent and overlying air, which would naturally lead to an early dissipation of the fog (Price et al., 2015). Fig. 7 shows a faster increase in horizontal wind speed after 10LT on 22 December compared to that on 23 December, which together with the faster increase in temperature and decrease in RH is consistent with an early termination of the fog event on that day.

Also plotted in Fig. 6 is the brightness temperature estimates from the IRTS. It allows us to diagnose the nature of the fog events, in particular if the fog formed by descending low-level clouds or at the surface directly by radiative cooling (radiation fog). During the fog periods, the brightness temperature is comparable to the air temperature indicating that fog is indeed present at the site. Before the onset and after the dissipation of the fog, there is a sudden increase and decrease of the brightness temperature, respectively, by about 10–30 °C. This indicates that the fog that occurred on the 22 and 23 December was predominantly of a radiative nature, the most common fog type in the region (e.g. de Villiers and van Heerden, 2007). The clearer skies enhance the surface radiative cooling, that together with reduced wind speeds help in the development of the fog (Smith et al., 2018). The rapid fluctuations in the brightness temperature on 24 December are probably due to the presence of scattered clouds, which is confirmed by an inspection of the satellite images (not shown). The analysis of the CBH from the IRTS showed that they are not capturing the dynamics of the fog onset and dissipation. The CBH from IRTS is inferred from the MWR temperature profile by finding the corresponding height of the IRTS temperature. A strong atmospheric attenuation could introduce a bias between the IRTS and MWR temperatures.

Table 2 shows the onset, dissipation time and duration of all fog events that have lasted for > 1 h and sensed by the MWR. These fog events are identified using METAR data and measurements from the

visibility sensor. The timing of the events is comparable when using observations taken at Abu Dhabi's International Airport and at the field site in Masdar Institute, which is expected given the close proximity of the two sites (roughly 4 km apart). In line with published work (Aldababseh and Temimi, 2017; de Villiers and van Heerden, 2007), longer-lasting fog events occur almost exclusively from December to February. The mean bias in air temperature and specific humidity for the 13 fog events (radiosonde data is not available for the 25 Dec 2017 fog case) are 0.03 K (0.09 K) and $-0.95\,g\,kg^{-1}$ ($0.62\,g\,kg^{-1}$) for the altitude < 2 km (> 2 km) respectively. Also shown in Table 2 are the mean visibility and PBL depth for the duration of each fog event. The averaged values over all 14 fog events are 0.298 ± 0.123 km and 0.060 ± 0.071 km, respectively. As expected, the visibility is < 1 km and the boundary layer is rather shallow, as fog takes place in a stable boundary layer (e.g. Bartok et al., 2012). There appears to be a weak positive correlation between the visibility and PBL height: when the boundary layer is shallower, the visibility is further reduced suggesting a more significant fog event. An interesting result from Table 2 is the gradual increase in fog duration on consecutive days from 6 to 10 February 2018, from roughly 1–2 h in the former to 7–9 h in the latter (events #7 to 10). In order to better understand what is behind this increase in the temporal extent of the fog, the MWR vertical profiles and surface weather measurements from 5 February at 10 LT to 12 February at 06 LT, a period which comprises the referred four fog events, are shown in Figs. 8 and 9.

In the analysis of 22 and 23 December 2017 fog events in Fig. 6, a strong correlation between the occurrence of fog and the strength of the near-surface temperature inversion was noted, with lapse rates in the lowest 250 m of up to $30\,K\,km^{-1}$ during fog events. For the period 5 to 12 February, while during the fog events the lapse rates were of a comparable magnitude, they were even steeper on 12 February when fog did not occur reaching up to $40\,K\,km^{-1}$. It is possible that on this day the inversion is so strong that it prevents the development of turbulence and subsequent formation of fog. This has been reported by other authors such as Zhang et al. (2008). The specific humidity profile suggests a link between the moistening of the near-surface atmosphere during the afternoon and early evening hours and the formation of fog in the following night that was not observed in the 22–23 December 2017 events. In particular, on 6, 7, 8 and 10 February when fog occurred, the atmosphere in the bottom 250 m was far more moist, with a deeper moist layer just above the surface, compared to the 9, 11 and 12 February when no fog formed. However, there are common features between the two sets of events: the downward mixing of the nocturnal residual layer in the morning hours; the subsidence above 2.5 km leading to warmer and drier conditions which at times descends to < 1.5 km and compresses the residual mixed-layer; the depletion of moisture just above the surface at night, possibly because of dew/fog occurrence as a result of the strong nighttime radiative cooling.

Fig. 9 shows the air temperature, relative humidity, and horizontal wind direction and speed measurements from the weather station at the field site. The fog that occurred during this period was of a predominantly radiative nature. In line with de Villiers and van Heerden (2007) and Chaouch et al. (2017), during daytime the sea-breeze (north to north-westerly winds) advected the more moist air from the Arabian Gulf inland, with the backing of the wind and reduced wind speed at night, coupled with a strong surface cooling with nighttime temperatures dropping to as low as 10 °C, leading to the formation of fog. Fig. 9 reveals that, while in no-fog days the nighttime relative humidity is generally below 80% in contrast with fog days when it exceeds 95%, the air temperature values for fog and no-fog days are comparable. This indicates that fog did not occur on 9, 11 and 12 February because of lower water vapour mixing ratios. One possible explanation is weaker advection of moisture from the Arabian Gulf: e.g. no fog formed on 12 February, and on 11 February the maximum daytime wind speed does not exceed $3\,m\,s^{-1}$ with more offshore winds compared to the 6, 7, 8 and 10 February when fog occurred. However, this is not the only reason for the drier near-surface atmosphere on the referred days. After all, the daytime wind speed and direction variability on 8 February are similar to that on 7 February but fog occurs on 8 February and does not form on 9 February. Fig. 8(c) shows a drier layer (specific

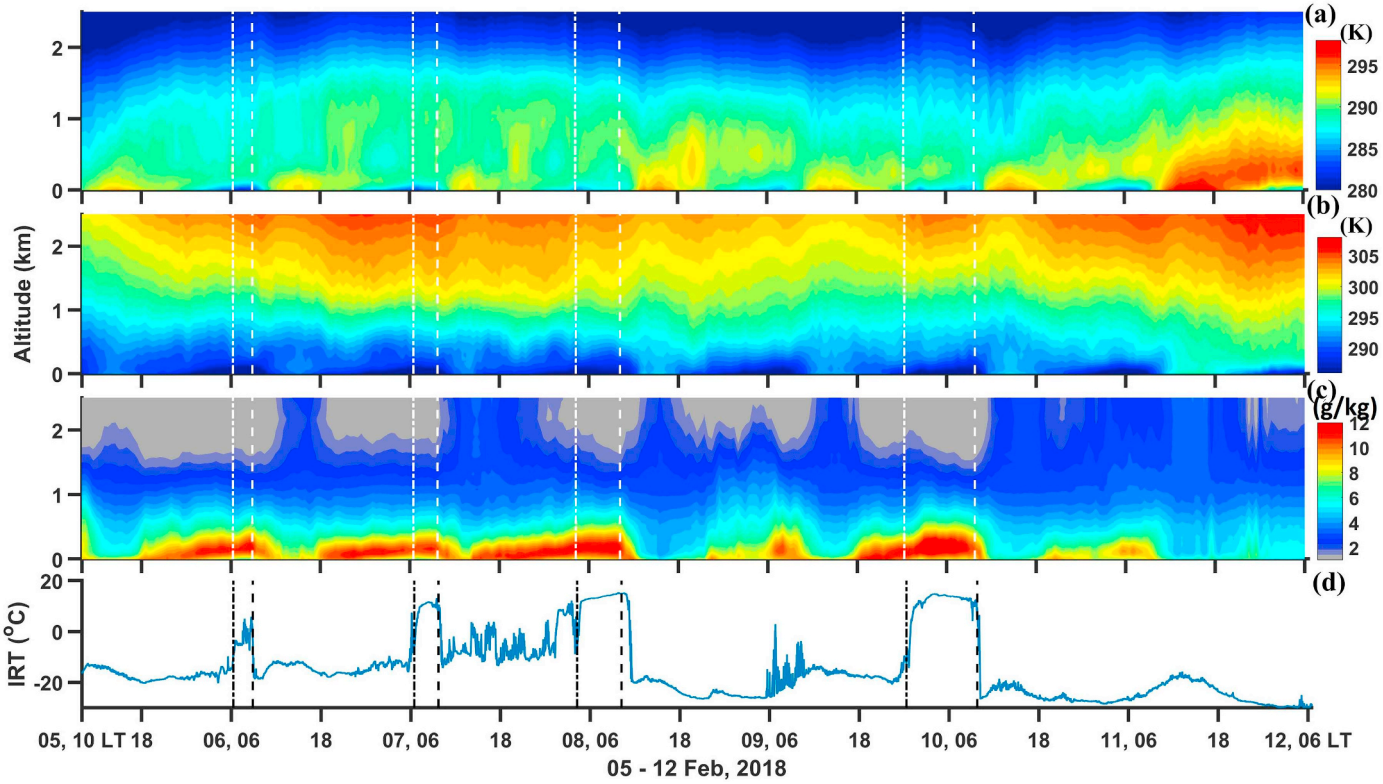

Fig. 8. As Fig. 6 but for the period 10 LT on 5 February to 06 LT on 12 February 2018.

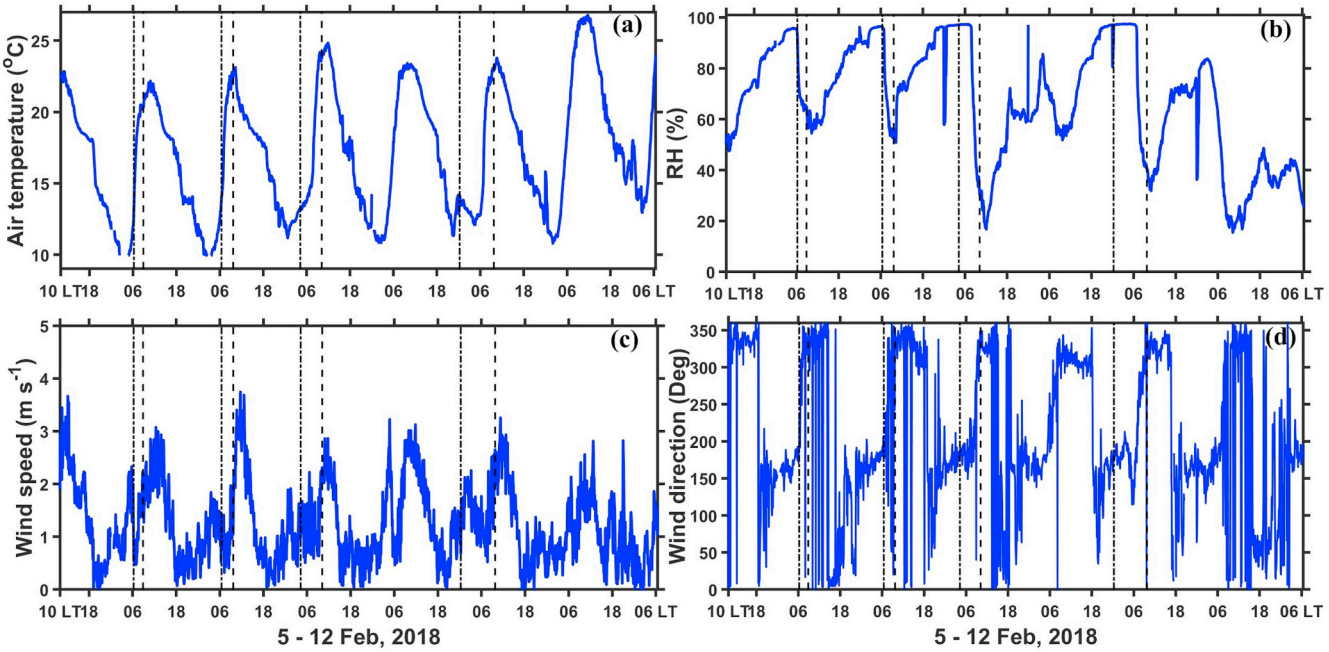

Fig. 9. As Fig. 7 but for the period 10 LT on 5 February to 06 LT on 12 February 2018.

humidity $< 5\,g\,kg^{-1}$) between roughly 250 m and 1 km in particular on 8, 10 and 11 February, which may prevent the deepening of the daytime mixed-layer and consequently the formation of fog. This layer probably arises from subsidence as it also features increased temperature values. Subsidence warming at night is known to promote the development of fog as it helps to create and maintain a low-level temperature inversion and subsequently trap moisture below (Koračin, 2017). In addition, drier air above the fog layer helps to cool it down by enhancing longwave radiative cooling at the fog top and vertical mixing below (Yang et al., 2018). However, the presence of a subsidence layer at very low levels during daytime may hinder fog development as it prevents the moistening of the near-surface atmosphere.

As was the case for the 22 and 23 December fog events, the fog that occurred on 6, 7 and 10 February was predominantly of a radiative nature, with comparable changes (typically 10–30 °C) in the brightness temperature immediately before and after the fog events. However, the fog event on 8 February resulted from the lowering of stratus clouds as evidenced by the smoother variation of the brightness temperature, Fig. 8(d), which is confirmed in an inspection of the satellite images (not shown).

In the previous discussion the focus was on the two fog events which occurred on 22 and 23 December 2017 and the four events which took place on 6, 7, 8 and 10 February 2018. In order to have a better understanding of the temporal evolution of the temperature and humidity fields during the development of fog, Fig. 10 shows the time-lagged tendencies averaged over all fog events, for a 32 h period centered in the middle of the foggy period.

Approximately 15 h before the peak of the fog, in the afternoon hours, there is an increase in the specific humidity in the bottom 250 m of the atmosphere with a weaker drying tendency aloft. As shown in Figs. 6–9, this is brought about by the sea breeze and moisture advection from the Arabian Gulf. Initially, the moistening tendency is at very low levels but it gradually moves upwards with time as a temperature inversion develops just above the surface (note the increase in the magnitude of the near-surface cooling from −7 to −2 h that is accompanied by a drying tendency). The presence of both a surface temperature inversion and sufficient moisture in the air are requirements for the occurrence of fog. While the buildup of fog is gradual, its termination is rather abrupt: when it dissipates, a very significant warming (in excess of $2\,K\,h^{-1}$) and drying (in excess of $1.2\,g\,kg^{-1}\,h^{-1}$) of the near-surface environment takes place. This corresponds to the erosion of the nighttime temperature inversion and increase in vertical mixing with the drier air above, as well as to the heating of the surface by the Sun. A similar trend is noted in Figs. 6 and 8. The time taken for the fog to clear depends on thickness of the fog layer, with a thicker layer taking longer to burn off with the warming at the fog top after sunrise, but also leading to more stable conditions near the surface. According to Fig. 10, the referred temperature and moisture tendencies occur from roughly 2 to 7 h after the peak of the fog, with only two of the 14 fog cases listed in Table 2 lasted for > 7 h. The near-surface temperature tendencies estimated from the MWR measurements are comparable to those reported by Dupont et al. (2016) during a fog event on 14 March 2014 in Paris. It is interesting to note that, while the highest temperature tendencies occur at the surface, the largest specific humidity tendencies are seen at about 250 m, where the daytime moistening is also the strongest. As daylight returns, the cycle repeats itself. In line with Figs. 7 and 9, the warming tendency in the surface temperature occurs in a shorter period of time during the morning hours (about 7 h) but at much higher rates in comparison to the cooling which lasts for more than ~17 h. The sudden changes in the magnitude of the temperature/humidity rates between +8 h to +11 h may arise from turbulent mixing. Fig. 10 provides a nice summary of the characteristics of the majority of the fog events at Abu Dhabi, which result from a combination of advective and radiative processes (de Villiers and van Heerden, 2007). It also confirms that the findings reached in the analyses of the December 2017 and February 2018 events are representative of fog events at Abu Dhabi.

Fig. 11 shows the averaged vertical profiles for all 14 fog events listed in Table 2. As expected, the near-surface temperature inversion is stronger in the cold season, in particular in the December 2017 and February 2018 events, when the nighttime radiative cooling is more significant. The February 2018 events were unusual in that the atmosphere in the bottom 2.5 km was rather cold, given the lack of subsidence warming above 1 km. Due to the lower temperatures, smaller amounts of water vapour mixing ratio are needed for condensation (and hence fog) to occur, which explains the lower q values of seen in Fig. 11(c). The subsidence is possibly associated with the subtropical anticyclones and associated large-scale descent and adiabatic warming.

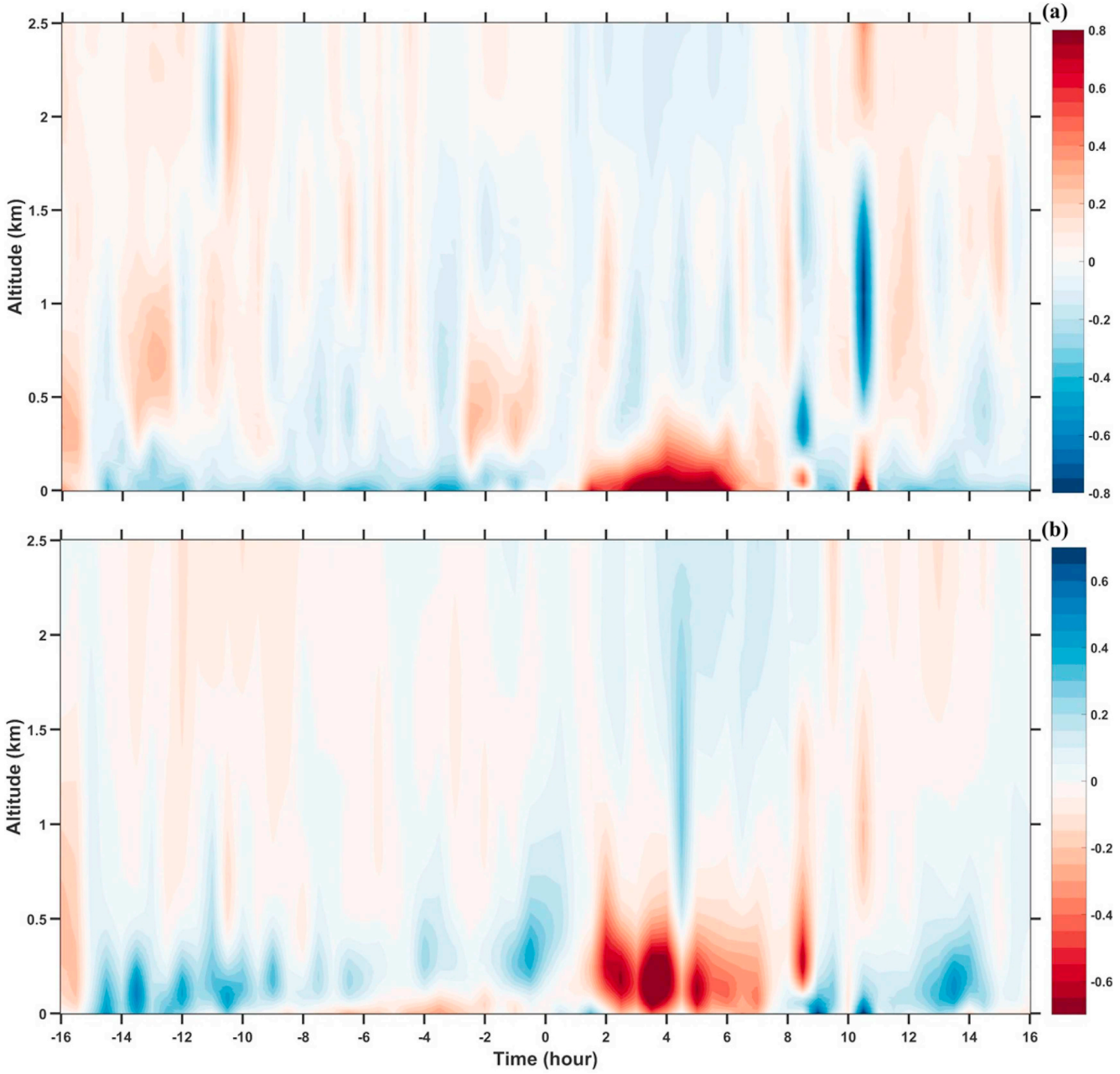

Fig. 10. Time-lagged composite of rate of change of temperature (K/30 min) and specific humidity (g kg^{-1}/30 min) for the 14 fog events listed in Table 2. Zero in the horizontal axis denotes the middle of the fog event.

This hypothesis is further supported by the fact that it is stronger during the spring season, descending to about 500 m in April, when the subtropical anticyclone has a larger effect on this region (e.g. Spinks et al., 2014). As noted previously, an increase in the near-surface water vapour mixing ratio during the afternoon and early evening hours by the sea-breeze circulation does not necessarily translate into the formation of fog in the following night. This can be seen by comparing the specific humidity values in the lowest 250 m for the December 2017 and February 2018 events. Hence, and as pointed out by published literature, other factors are important for fog formation such as the strength of the temperature inversion and the horizontal wind speed (e.g. de Villiers and van Heerden, 2007; Lyons, 2018). Having said that, a water vapour mixing ratio in excess of 6 g kg^{-1} just above the surface seems to be needed for fog to form. Fig. 11 highlights that there is some monthly/seasonal variability in the atmospheric state during fog events at this site.

5. Summary

A MWR was installed at Masdar Institute in Abu Dhabi, roughly 4 km from the airport, with measurements taken for the periods 18 February to 23 April 2017, 2 November 2017 to 12 May 2018, and 6 February to 31 March 2019. It provides temperature and humidity profiles, with 31 levels in the lowest 1 km of the atmosphere, that are used for the present analysis. In addition to the MWR, an IRTS, which gives estimates of cloud base height and cloud liquid water, an integrated automatic weather station, and a visibility sensor are also available at the site.

The MWR temperature is in close agreement with that from radiosonde, generally within 1 K. The specific humidity biases, on the other hand, are of a larger magnitude, of up to 5 g kg^{-1}. The drier and slightly warmer radiosonde profile in the mid-troposphere can be attributed to the known effect of the solar heating on the humidity sensor in the

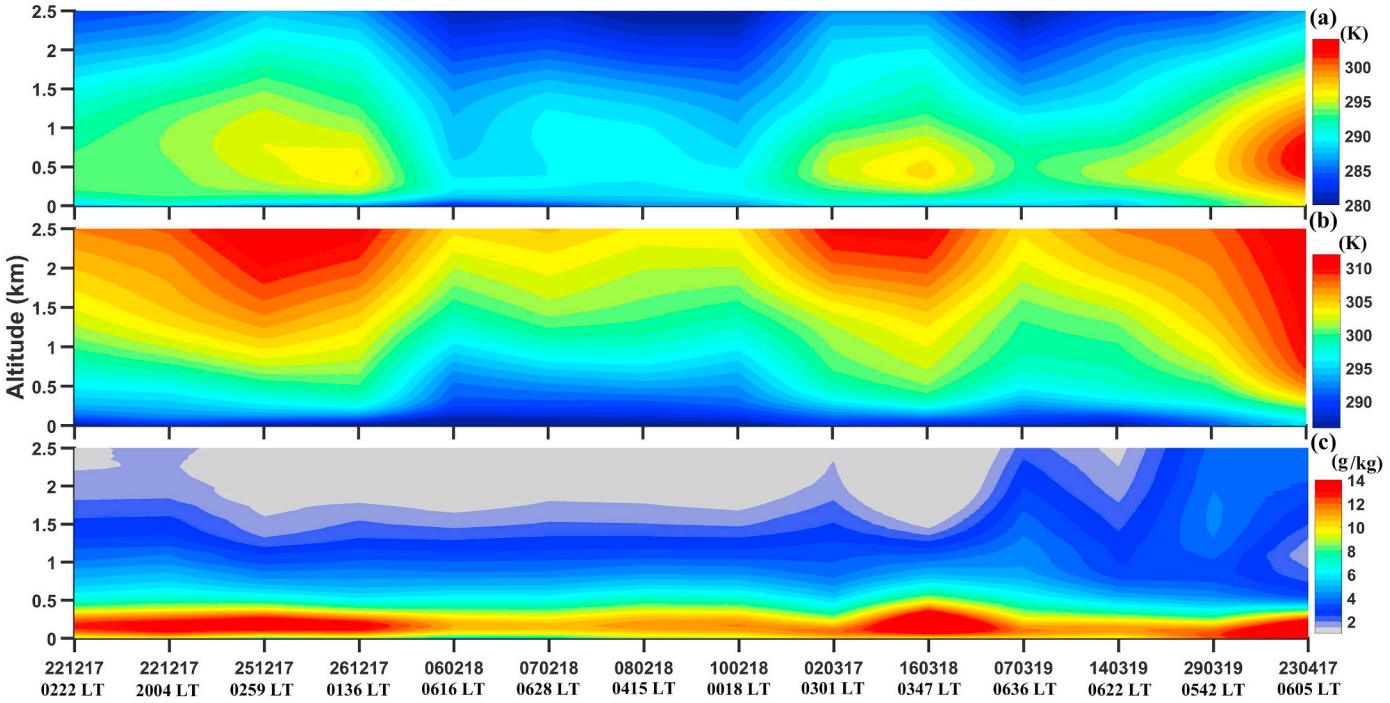

Fig. 11. Average (a) temperature (K), (b) potential temperature (K) and (c) specific humidity (g kg^{-1}) vertical profiles for the bottom 2.5 km of the atmosphere for the 14 fog events listed in Table 2. For a given event, the profiles are averaged over all fog hours. For events #1 and 2, the onset and dissipation times are taken from the METAR data, for the rest the visibility sensor estimates are used to define the extent of the fog event.

radiosonde (e.g. Vömel et al., 2007). An analysis of the seasonality of the temperature and specific humidity biases revealed that, while the latter are very similar for the different months considered, the former shows an increasing trend being mostly negative from November to January, and mostly positive in March and April. This may be related to the changes in the atmosphere from winter to spring and their impact on the performance of the retrieval algorithm.

An analysis of the vertical profiles of temperature and humidity for a typical day at the site revealed features commonly seen in arid/semi-arid regions such as a strong temperature inversion at night and a super adiabatic lapse rate in the early morning, followed by a well-mixed atmosphere in the late morning and early afternoon. The daytime PBL depths are lower than at other arid sites (e.g. Garcia-Carreras et al., 2015; Wang et al., 2016), which has been attributed to the more moist atmosphere at Abu Dhabi (e.g. Eager et al., 2008; Xue and Eltahir, 2015).

The MWR data are also used to better understand the changes in the atmospheric profiles during fog events, which are common in Abu Dhabi in particular in the cold season (Aldababseh and Temimi, 2017). Two consecutive fog events on 22 and 23 December 2017 and four events with an increasing temporal extent on 6, 7, 8 and 10 February 2018 are investigated.

In line with previous work, it is found that a strong near-surface temperature inversion of up to 30 K km^{-1} in the bottom 250 m is needed for fog to form (e.g. RenHe et al., 2014). However, if it is too strong, here up to 40 K km^{-1}, it may prevent its development (Zhang et al., 2018). The moistening of the atmosphere in the bottom 500 m is a necessary but not sufficient condition for the development of fog, with a water vapour mixing ratio of at least 6 g kg^{-1} just above the surface present in all 14 fog events considered. The near-surface water vapour mixing ratio starts to increase in the late morning and early afternoon as the sea-breeze carries the more moist air from the Arabian Gulf inland (Chaouch et al., 2017; Weston et al., 2018). As the thermal inversion develops, roughly 3 to 5 h before the onset of fog, the more moist near-surface air is advected upwards, above the inversion. When it is destroyed in the morning, the nocturnal residual layer mixes down to the surface. Such a behavior has been pointed out by other authors like Muñoz and Undurraga (2010). A common feature observed in the MWR profiles is subsidence warming and drying generally above 1.5 km, that is more significant in the spring and summer seasons. It is a ubiquitous feature in the region that originates from the quasi-permanent presence of the subtropical anticyclones (e.g. Seager et al., 2003).

Potential future applications of the MWR measurements are: (i) assimilation into the operational model runs; (ii) evaluation of the performance of numerical models as done e.g. in Cossu et al. (2015); (iii) used to estimate fog indicators such as the Fog Stability Index (Arun et al., 2018; Cimini et al., 2015), which may help in the prediction of fog. Furthermore, analysis of the measurements and numerical simulations showed that fog development and dissipation are sensitive to other key variables that the MWR is not retrieving like the droplet-size distribution. This suggests that the MWR in the context of fog studies should be integrated with a suite of other instruments for detailed understanding of the processes controlling fog formation and dissipation. Some of these results will be shown in a subsequent paper.

Data availability

All data needed to evaluate the conclusions in the paper are presented in the paper and/or the Supplement. Additional data related to this paper may be requested from the authors.

Declaration of Competing Interest

The authors declare no conflicts of interest.

Acknowledgments

We acknowledge the National Center of Meteorology (NCM) for kindly providing radiosonde data at Abu Dhabi's International Airport through the University of Wyoming website which were used in this work for the evaluation of the Microwave Radiometer performance.

Appendix A. Supplementary data

Supplementary data to this article can be found online at https://doi.org/10.1016/j.atmosres.2019.104652.

References

Al Azhar, M., Temimi, M., Zhao, J., Ghedira, H., 2016. Modeling of the circulation in the Arabian Gulf and the Sea of Oman: skill assessment and seasonal thermohaline structure. J. Geophys. Res. Oceans 121, 1700–1720. https://doi.org/10.1002/2015JC011038.

Al Jassar, H.K., Temimi, M., Entekhabi, D., Petrov, P., Al Sarraf, H., Kokkalis, P., Roshni, N., 2019. Forward simulation of multi-frequency microwave brightness temperature over desert soils in Kuwait and comparison with satellite observations. Remote Sens. 11, 1647. https://doi.org/10.3390/rs11141647.

Aldababseh, A., Temimi, M., 2017. Analysis of the long-term variability of poor visibility events in the UAE and the link with climate dynamics. Atmos 8, 242. https://doi.org/10.3390/atmos8120242.

Ali, O.W.B., Al-Harthei, H., Garib, A., 2013. Real-Time fog warning system for the Abu Dhabi Emirate (UAE). J. Traffic Transp. Eng. 1, 213–217. https://doi.org/10.12720/jtle.1.2.213-217.

Arun, S.H., Chaurasia, S., Misra, A., Kumar, R., 2018. Fog stability index: a novel technique for fog/low clouds detection using multi-satellites data over the Indo-Gangetic plains during winter season. Int. J. Remote Sens. 39, 8200–8218. https://doi.org/10.1080/01431161.2018.1483085.

Balaji, B., Prabha, T.V., Jaya Rao, Y., Kiran, T., Dinesh, G., Chakravarty, K., Sonbawne, S.M., Rajeevan, M., 2017. Potential of collocated radiometer and wind profiler observations for monsoon studies. Atmos. Res. 194, 17–26. https://doi.org/10.1016/j.atmosres.2017.04.023.

Bartok, J., Bott, A., Gera, M., 2012. Fog prediction for road traffic safety in a coastal desert region. Boundary-Layer Meteorol. 145, 485–506. https://doi.org/10.1007/s10546-012-9750-5.

Basha, G., Ratnam, M.V., 2009. Identification of atmospheric boundary layer height over a tropical station using high-resolution radiosonde refractivity profiles: Comparison with GPS radio occultation measurements. J. Geophys. Res. 114, D16101. https://doi.org/10.1029/2008jd011692.

Bennartz, R., Bauer, P., 2003. Sensitivity of microwave radiances at 85-183 GHz to precipitating ice particles. Radio Sci. 38, 8075. https://doi.org/10.1029/2002rs002626.

Blackwell, W.J.C., Chen, Frederick W., 2009. Neural Networks in Atmospheric Remote Sensing. Artech House Remote Sensing Library (234 pp).

Blay-Carreras, E., Pino, D., Vilà-Guerau de Arellano, J., van de Boer, A., De Coster, O., Darbieu, C., Hartogensis, O., Lohou, F., Lothon, M., Pietersen, H., 2014. Role of the residual layer and large-scale subsidence on the development and evolution of the convective boundary layer. Atmos. Chem. Phys. 14, 4515–4530. https://doi.org/10.5194/acp-14-4515-2014.

Cadeddu, M.P., Liljegren, J.C., Pazmany, A., 2006. Measurements and retrievals from a New 183-GHz water vapor radiometer in the Arctic. In: Conference Paper, 2006 IEEE MicroRad, SanJuan, Puerto Rico. IEEE, pp. 252–255. https://doi.org/10.1109/MICRAD.2006.1677098.

Cady-Pereira, K.E., Shephard, M.W., Turner, D.D., Mlawer, E.J., Clough, S.A., Wagner, T.J., 2008. Improved daytime column-integrated precipitable water vapor from Vaisala radiosonde humidity sensors. J. Atmos. Ocean. Technol. 25, 873–883. https://doi.org/10.1175/2007jtecha1027.1.

Chakraborty, R., Maitra, A., 2016. Retrieval of atmospheric properties with radiometric measurements using neural network. Atmos. Res. 181, 124–132. https://doi.org/10.1016/j.atmosres.2016.05.011.

Chan, P.W., 2009. Performance and application of a multi-wavelength, ground-based microwave radiometer in intense convective weather. Met. Ze. 18, 253–265. https://doi.org/10.1127/0941-2948/2009/0375.

Chan, P.W., Hon, K.K., 2011. Application of ground-based, multi-channel microwave radiometer in the nowcasting of intense convective weather through instability indices of the atmosphere. Met. Ze. 20, 431–440. https://doi.org/10.1127/0941-2948/2011/0276.

Chan, P.W., Li, C.M., 2010. Application of a ground-based microwave radiometer in cloud observations. In: Conference Proceedings, 11th Specialist Meeting on Microwave Radiometry and Remote Sensing of the Environment, Washington, D. C.,United States of America, . https://www.hko.gov.hk/publica/reprint/r890.pdf.

Chan, P.W., Li, Q.S., 2018. Case studies of springtime fog in Hong Kong. Weather 74, 60–67. https://doi.org/10.1002/wea.3277.

Chaouch, N., Temimi, M., Weston, M., Ghedira, H., 2017. Sensitivity of the meteorological model WRF-ARW to planetary boundary layer schemes during fog conditions in a coastal arid region. Atmos. Res. 187, 106–127. https://doi.org/10.1016/j.atmosres.2016.12.009.

Cimini, D., De Angelis, F., Dupont, J.C., Pal, S., Haeffelin, M., 2013. Mixing layer height retrievals by multichannel microwave radiometer observations. Atmos. Meas. Tech. 6, 2941–2951. https://doi.org/10.5194/amt-6-2941-2013.

Cimini, D., Nelson, M., Güldner, J., Ware, R., 2015. Forecast indices from a ground-based microwave radiometer for operational meteorology. Atmos. Meas. Tech. 8, 315–333. https://doi.org/10.5194/amt-8-315-2015.

Cossu, F., Hocke, K., Martynov, A., Martius, O., Mätzler, C., 2015. Atmospheric water parameters measured by a ground-based microwave radiometer and compared with the WRF model. Atmos. Sci. Lett. 16, 465–472. https://doi.org/10.1002/asl.583.

Crewell, S., Czekala, H., Lohnert, U., Simmer, C., Rose, T., Zimmermann, R., Zimmermann, R., 2001. Microwave radiometer for cloud carthography: a 22-channel ground-based microwave radiometer for atmospheric research. Radio Sci. 36, 621–638. https://doi.org/10.1029/2000RS002396.

de Villiers, M.P., van Heerden, J., 2007. Fog at Abu Dhabi International Airport. Weather. 62, 209–214. https://doi.org/10.1002/wea.45.

Dee, D.P., Uppala, S.M., Simmons, A.J., Berrisford, P., Poli, P., Kobayashi, S., Andrae, U., Balmaseda, M.A., Balsamo, G., Bauer, P., Bechtold, P., Beljaars, A.C.M., van de Berg, L., Bidlot, J., Bormann, N., Delsol, C., Dragani, R., Fuentes, M., Geer, A.J., Haimberger, L., Healy, S.B., Hersbach, H., Hólm, E.V., Isaksen, L., Kållberg, P., Köhler, M., Matricardi, M., McNally, A.P., Monge-Sanz, B.M., Morcrette, J.J., Park, B.K., Peubey, C., de Rosnay, P., Tavolato, C., Thépaut, J.N., Vitart, F., 2011. The ERA-Interim reanalysis: configuration and performance of the data assimilation system. Q. J. R. Meteorol. Soc. 137, 553–597. https://doi.org/10.1002/qj.828.

Dupont, J.C., Haeffelin, M., Badosa, J., Elias, T., Favez, O., Petit, J.E., Meleux, F., Sciare, J., Crenn, V., Bonne, J.L., 2016. Role of the boundary layer dynamics effects on an extreme air pollution event in Paris. Atmos. Environ. 141, 571–579. https://doi.org/10.1016/j.atmosenv.2016.06.061.

Eager, R.E., Raman, S., Wootten, A., Westphal, D.L., Reid, J.S., Al Mandoos, A., 2008. A climatological study of the sea and land breezes in the Arabian Gulf region. J. Geophys. Res. 113, D15106. https://doi.org/10.1029/2007jd009710.

Eltahir, E.A.B., 1998. A soil moisture–rainfall feedback mechanism: 1. Theory and observations. Water Resour. Res. 34, 765–776. https://doi.org/10.1029/97WR03499.

Fares, A., Temimi, M., Morgan, K., Kelleners, T.J., 2013. In-Situ and remote soil moisture sensing technologies for Vadose Zone Hydrology. Vadose Zone J. 12. https://doi.org/10.2136/vzj2013.03.0058.

Feltz, W.F., Smith, W.L., Howell, H.B., Knuteson, R.O., Woolf, H., Revercomb, H.E., 2003. Near-continuous profiling of temperature, moisture, and atmospheric stability using the Atmospheric Emitted Radiance Interferometer (AERI). J. Appl. Meteorol. 42, 584–597. https://doi.org/10.1175/1520-0450(2003)042<0584:NPOTMA>2.0.CO;2.

Fochesatto, G.J., Drobinski, P., Flamant, C., Guedalia, D., Sarrat, C., Flamant, P.H., Pelon, J., 2001. Evidence of dynamical coupling between the residual layer and the developing convective boundary layer. Boundary-Layer Meteorol. 99, 451–464. https://doi.org/10.1023/a:1018935129006.

Foster, M.J., Heidinger, A., 2012. PATMOS-x: results from a diurnally corrected 30-yr satellite cloud climatology. J. Clim. 26, 414–425. https://doi.org/10.1175/JCLI-D-11-00666.1.

Garcia-Carreras, L., Parker, D.J., Marsham, J.H., Rosenberg, P.D., Brooks, I.M., Lock, A.P., Marenco, F., McQuaid, J.B., Hobby, M., 2015. The turbulent structure and diurnal growth of the Saharan atmospheric boundary layer. J. Atmos. Sci. 72, 693–713. https://doi.org/10.1175/jas-d-13-0384.1.

Garratt, J.R., 1992. The Atmospheric Boundary Layer. Cambridge Univ. Press, Cambridge, U.K.

Haeffelin, M., Bergot, T., Elias, T., Tardif, R., Carrer, D., Chazette, P., Colomb, M., Drobinski, P., Dupont, E., Dupont, J.C., Gomes, L., Musson-Genon, L., Pietras, C., Plana-Fattori, A., Protat, A., Rangognio, J., Raut, J.C., Rémy, S., Richard, D., Sciare, J., Zhang, X., 2010. Parisfog. Bull. Am. Meteorol. Soc. 91, 767–783. https://doi.org/10.1175/2009bams2671.1.

HATPRO, 2019. Humidity And Temperature PROfilers. https://www.radiometer-physics.de/products/microwave-remote-sensing-instruments/radiometers/humidity-and-temperature-profilers/, Accessed date: 12 May 2019.

Jacobs, A.F.G., Heusinkveld, B.G., Berkowicz, S.M., 2000. Force-restore technique for ground surface temperature and moisture content in a dry desert system. Water Resour. Res. 36, 1261–1268. https://doi.org/10.1029/2000wr900016.

John, V.O., Buehler, S.A., 2005. Comparison of microwave satellite humidity data and radiosonde profiles: a survey of European stations. Atmos. Chem. Phys. 5, 1843–1853. https://doi.org/10.5194/acp-5-1843-2005.

Jung, T., Ruprecht, E., Wagner, F., 1998. Determination of cloud liquid water path over the oceans from special Sensor Microwave/Imager (SSM/I) DATA using neural networks. J. Appl. Meteorol. 37, 832–844. https://doi.org/10.1175/1520-0450(1998)037<0832:doclwp>2.0.co;2.

Karstens, U., Simmer, C., Ruprecht, E., 1994. Remote sensing of cloud liquid water. MAP 54, 157–171. https://doi.org/10.1007/bf01030057.

Knupp, K.R., Coleman, T., Phillips, D., Ware, R., Cimini, D., Vandenberghe, F., Vivekanandan, J., Westwater, E., 2009. Ground-based passive microwave profiling during dynamic weather conditions. J. Atmos. Ocean. Technol. 26, 1057–1073. https://doi.org/10.1175/2008jtecha1150.1.

Koračin, D., 2017. Modeling and forecasting marine fog. In: Koračin, D., Dorman, C. (Eds.), Marine Fog: Challenges and Advancements in Observations, Modeling, and Forecasting. Springer Atmospheric Sciences, pp. 425–475.

Kumar, M., Mallik, C., Kumar, A., Mahanti, N.C., Shekh, A.M., 2010. Evaluation of the boundary layer depth in semi-arid region of India. Dyn. Atmos. Oceans 49, 96–107. https://doi.org/10.1016/j.dynatmoce.2009.01.002.

Lazzarini, M., Marpu, P.R., Eissa, Y., Ghedira, H., 2014. Toward a near real-time product of air temperature maps from satellite data and *in Situ* measurements in arid environments. IEEE J. Sel. Top. Appl. Earth Obs. Remote Sens. 7, 3093–3104. https://doi.org/10.1109/jstars.2014.2320762.

Lyons, W., 2018. Unraveling the mysteries of fog. Weatherwise 71, 32–39. https://doi.org/10.1080/00431672.2018.1514188.

Madhulatha, A., Rajeevan, M., Venkat Ratnam, M., Bhate, J., Naidu, C.V., 2013. Nowcasting severe convective activity over southeast India using ground-based microwave radiometer observations. J. Geophys. Res. Atmos. 118, 1–13. https://doi.org/10.1029/2012jd018174.

Meyer, M.B., Lala, G.G., 1990. Climatological aspects of radiation fog occurrence at Albany, New York. J. Clim. 3, 577–586. https://doi.org/10.1175/1520-0442(1990)003<0577:CAORFO>2.0.CO;2.

Ming, H., Wei, M., Wang, M., Gao, L., Chen, L., Wang, X., 2019. Analysis of fog at

Xianyang Airport based on multi-source ground-based detection data. Atmos. Res. 220, 34–45. https://doi.org/10.1016/j.atmosres.2019.01.012.
Muñoz, R.C., Undurraga, A.A., 2010. Daytime mixed layer over the Santiago Basin: description of two years of observations with a lidar ceilometer. J. Appl. Meteorol. Climatol. 49, 1728–1741. https://doi.org/10.1175/2010jamc2347.1.
Nehrkorn, T., Grassotti, C., 2003. Mesoscale variational assimilation of profiling radiometer data. In: Conference Proceedings, 20th Conf. on Weather Analysis and Forecasting/16th Conf. on Numerical Weather Prediction, Seattle, WA.
Panda, S., Sahoo, S., Pandithurai, G., 2017. Time series analysis of ground-based microwave measurements at K- and V-bands to detect temporal changes in water vapor and temperature profiles. Geosci. Instrum. Methods Data Syst. 6, 15–26. https://doi.org/10.5194/gi-6-15-2017.
Payra, S., Mohan, M., 2014. Multirule based diagnostic approach for the fog predictions using WRF modelling tool. Adv. Meteorol. 2014, 1–11. https://doi.org/10.1155/2014/456065.
Picón-Feliciano, A.J., Vásquez, R., Gonzalez, J., Luvall, J., Rickman, D., 2009. Use of Remote Sensing Observations to Study the Urban Climate on Tropical Coastal Cities. (Rev Umbral).
Price, J., Porson, A., Lock, A., 2015. An observational case study of persistent fog and comparison with an ensemble forecast model. Boundary-Layer Meteorol. 155, 301–327. https://doi.org/10.1007/s10546-014-9995-2.
Qiang, Z., Sheng, W., 2009. A study of the atmospheric boundary layer structure during a clear day in the arid region of Northwest China. J. Meteor. Res. 23, 327–337.
Qiang, Z., Sheng, W., Yanying, L., 2006. Study on physical mechanism of influence on atmospheric boundary layer depth in the arid regions of Northwest China. J. Meteor. Res. 20, 1–12.
Ratnam, M.V., Santhi, Y.D., Rajeevan, M., Rao, S.V.B., 2013. Diurnal variability of stability indices observed using radiosonde observations over a tropical station: comparison with microwave radiometer measurements. Atmos. Res. 124, 21–33. https://doi.org/10.1016/j.atmosres.2012.12.007.
RenHe, Z., Li, Q., Zhang, R., 2014. Meteorological conditions for the persistent severe fog and haze event over eastern China in January 2013. Sci. China Earth Sci. 57, 26–35. https://doi.org/10.1007/s11430-013-4774-3.
Rose, T., Crewell, S., Löhnert, U., Simmer, C., 2005. A network suitable microwave radiometer for operational monitoring of the cloudy atmosphere. Atmos. Res. 75, 183–200. https://doi.org/10.1016/j.atmosres.2004.12.005.
RPG, 2019. Instrument Operation and Software Guide. https://www.radiometer-physics.de/download/PDF/Radiometers/HATPRO/RPG_MWR_STD_Software_Manual%20G5.pdf, Accessed date: 12 May 2019.
Seager, R., Murtugudde, R., Naik, N., Clement, A., Gordon, N., Miller, J., 2003. Air–sea interaction and the seasonal cycle of the subtropical anticyclones*. J. Clim. 16, 1948–1966. https://doi.org/10.1175/1520-0442(2003)016<1948:aiatsc>2.0.co;2.
Seidel, D.J., Ao, C.O., Li, K., 2010. Estimating climatological planetary boundary layer heights from radiosonde observations: comparison of methods and uncertainty analysis. J. Geophys. Res. 115. https://doi.org/10.1029/2009jd013680.
SENTRY™, 2019. Visibility Sensor User's Guide. http://www.duranelectronica.com/english/wp-content/uploads/2015/12/I-SVS1-T-Users-Guide-Jan-2013-opac-v02.pdf, Accessed date: 12 May 2019.
Smith, D.K.E., Renfrew, I.A., Price, J.D., Dorling, S.R., 2018. Numerical modelling of the evolution of the boundary layer during a radiation fog event. Weather 73, 310–316. https://doi.org/10.1002/wea.3305.
Spinks, J., Lin, Y.-L., Mekonnen, A., 2014. Effects of the subtropical anticyclones over North Africa and Arabian Peninsula on the African easterly jet. Int. J. Climatol. 35, 733–745. https://doi.org/10.1002/joc.4017.
Temimi, M., Lakhankar, T., Zhan, X., Cosh, M.H., Krakauer, N., Fares, A., Kelly, V., Khanbilvardi, R., Kumassi, L., 2014. Soil moisture retrieval using ground-based L-band passive microwave observations in Northeastern USA. Vadose Zone J. 13. https://doi.org/10.2136/vzj2013.06.0101.
Turner, D.D., Lesht, B.M., Clough, S.A., Liljegren, J.C., Revercomb, H.E., Tobin, D.C., 2003. Dry Bias and variability in Vaisala RS80-H radiosondes: the ARM experience. J. Atmos. Ocean. Technol. 20, 117–132. https://doi.org/10.1175/1520-0426(2003)020<0117:dbaviv>2.0.co;2.
Uwe, P., Rainer, H., Bodo, A., 2012. Cloud cover diurnal cycles in satellite data and regional climate model simulations. Met. Ze. 21, 551–560. https://doi.org/10.1127/0941-2948/2012/0423.
Vömel, H., Selkirk, H., Miloshevich, L., Valverde-Canossa, J., Valdés, J., Kyrö, E., Kivi, R., Stolz, W., Peng, G., Diaz, J.A., 2007. Radiation dry bias of the Vaisala RS92 humidity sensor. J. Atmos. Ocean. Technol. 24, 953–963. https://doi.org/10.1175/jtech2019.1.
Wærsted, E.G., Haeffelin, M., Dupont, J.-C., Delanoë, J., Dubuisson, P., 2017. Radiation in fog: quantification of the impact on fog liquid water based on ground-based remote sensing. Atmos. Chem. Phys. 17, 10811–10835. https://doi.org/10.5194/acp-17-10811-2017.
Wang, M., Wei, W., He, Q., Yang, Y., Fan, L., Zhang, J., 2016. Summer atmospheric boundary layer structure in the hinterland of Taklimakan Desert, China. J. Arid Land 8, 846–860. https://doi.org/10.1007/s40333-016-0054-3.
Wang, Z., Wang, Z., Cao, X., Mao, J., Tao, F., Hu, S., 2018. Cloud-base height derived from a ground-based infrared sensor and a comparison with a collocated cloud radar. J. Atmos. Ocean. Technol. 35, 689–704. https://doi.org/10.1175/jtech-d-17-0107.1.
Wehbe, Y., Ghebreyesus, D., Temimi, M., Milewski, A., Al Mandous, A., 2017. Assessment of the consistency among global precipitation products over the United Arab Emirates. J. Hydrol. Reg. Stud. 12, 122–135. https://doi.org/10.1016/j.ejrh.2017.05.002.
Wehbe, Y., Temimi, M., Weston, M., Chaouch, N., Branch, O., Schwitalla, T., Wulfmeyer, V., Al Mandous, A., 2018. Analysis of an extreme weather event in a hyper arid region using WRF-Hydro coupling, station, and satellite data. Nat. Hazards Earth Syst. Sci. 2018, 1–34. https://doi.org/10.5194/nhess-2018-226.
Wehbe, Y., Temimi, M., Weston, M., Chaouch, N., Branch, O., Schwitalla, T., Wulfmeyer, V., Zhan, X., Liu, J., Al Mandous, A., 2019. Analysis of an extreme weather event in a hyper-arid region using WRF-Hydro coupling, station, and satellite data. Nat. Hazards Earth Syst. Sci. 19, 1129–1149. https://doi.org/10.5149/nhess-19-1129-2019.
Weston, M., Chaouch, N., Valappil, V., Temimi, M., Ek, M., Zheng, W., 2018. Assessment of the sensitivity to the thermal roughness length in Noah and Noah-MP land surface model using WRF in an arid region. PApGe. https://doi.org/10.1007/s00024-018-1901-2.
Westwater, E.R., Stankov, B.B., Cimini, D., Han, Y., Shaw, J.A., Lesht, B.M., Long, C.N., 2003. Radiosonde humidity soundings and microwave radiometers during Nauru99. J. Atmos. Ocean. Technol. 20, 953–971. https://doi.org/10.1175/1520-0426(2003)20<953:rhsamr>2.0.co;2.
WS600-UMB, 2019. Smart Weather Sensor. https://www.lufft.com/products/compact-weather-sensors-293/ws600-umb-smart-weather-sensor-1832/, Accessed date: 12 May 2019.
Wyoming, U.o, 2019. Atmospheric Soundings. http://weather.uwyo.edu/upperair/sounding.html, Accessed date: 12 May 2019.
Xue, P., Eltahir, E.A.B., 2015. Estimation of the heat and water budgets of the Persian (Arabian) Gulf using a regional climate model. J. Clim. 28, 5041–5062. https://doi.org/10.1175/jcli-d-14-00189.1.
Yang, L., Liu, J.-W., Ren, Z.-P., Xie, S.-P., Zhang, S.-P., Gao, S.-H., 2018. Atmospheric conditions for advection-radiation fog over the Western Yellow Sea. J. Geophys. Res. Atmos. 123, 5455–5468. https://doi.org/10.1029/2017jd028088.
Ying, H.J., Sheng Wei, Z., Yu, Z., 2011. The primary design of advanced ground-based atmospheric microwave sounder and retrieval of physical parameters. J. Quant. Spectrosc. Radiat. Transf. 112, 236–246. https://doi.org/10.1016/j.jqsrt.2010.05.021.
Yousef, L.A., Temimi, M., Wehbe, Y., Al Mandous, A., 2019. Total cloud cover climatology over the United Arab Emirates. Atmos. Sci. Lett. 20, e883. https://doi.org/10.1002/asl.883.
Zaitsev, N.A., Timofeyev, Y.M., Kostsov, V.S., 2014. Comparison of radio sounding and ground-based remote measurements of temperature profiles in the troposphere. Atom. Ocean. Opt. 27, 386–392. https://doi.org/10.1134/S1024856014050169.
Zhang, S., Ren, Z., Liu, J., Yang, Y., Wang, X., 2008. Variations in the lower level of the PBL associated with the Yellow Sea fog-new observations by L-band radar. J. Ocean Univ. China 7, 353–361. https://doi.org/10.1007/s11802-008-0353-1.
Zhang, S.-P., Xie, S.-P., Liu, Q.-Y., Yang, Y.-Q., Wang, X.-G., Ren, Z.-P., 2009. Seasonal variations of yellow sea fog: observations and mechanisms. J. Clim. 22, 6758–6772. https://doi.org/10.1175/2009jcli2806.1.
Zhang, Q., Zhang, J., Qiao, J., Wang, S., 2011. Relationship of atmospheric boundary layer depth with thermodynamic processes at the land surface in arid regions of China. Sci. China Earth Sci. 54, 1586–1594. https://doi.org/10.1007/s11430-011-4207-0.
Zhang, J., Zuidema, P., Turner, D.D., Cadeddu, M.P., 2018. Surface-based microwave humidity retrievals over the equatorial Indian Ocean: applications and challenges. J. Appl. Meteorol. Climatol. 57, 1765–1782. https://doi.org/10.1175/jamc-d-17-0301.1.